

Chapter 2

Excitation of molecules in dense clouds

We present theoretical predictions of the strength of molecular lines under conditions suitable for dense molecular clouds including photon-dominated regions (PDRs) and star forming regions. These predictions are obtained by solving the statistical equilibrium equations and the radiative transfer using the escape probability method. Excitation and de-excitation through collisions with molecular hydrogen and free electrons are taken into account, as well as the effects of the radiation field, to which the molecular lines can contribute themselves.

It is found that rotational transitions of simple molecules are excellent tools to study the temperature and density under the conditions present in such clouds. The theoretical results are compared with observational data for the young stellar object IRAS 16293–2422 to show the diagnostic value of these millimeter and submillimeter lines.

To be submitted in modified form to A&A Suppl. by Jansen, Van Dishoeck and Black

1. Introduction

Observations of rotational transitions of interstellar molecules not only contain information about their abundance, but also on the excitation conditions. Specifically, the intensity ratio of two lines of the same molecule is, in the optically thin case, independent of the abundance of the molecule and can therefore be an excellent diagnostic of the physical conditions, such as kinetic temperature and density.

Ever since their discovery, molecules have been used to probe the physical conditions of the interstellar medium. Evans (1980) reviews the temperature and density diagnostics available at that time. As temperature tracers, the optically thick, thermalized ^{12}CO $1 \rightarrow 0$ line, and the NH_3 inversion doublets were used. The density was probed using the low-lying transitions of CS and HC_3N and the 2 cm and 2mm H_2CO lines, but this work had only just begun, after reliable collision rates had been published by Green et al. (1978). More temperature and density tracers became available when telescopes and receivers operating above 200 GHz were constructed and higher frequency transitions of molecules like formaldehyde became readily observable (see Walmsley 1987). An excellent overview of the diagnostic capabilities of atomic and molecular lines is given by Genzel (1992).

In recent years large aperture submillimeter telescopes, such as the James Clerk Maxwell Telescope (JCMT) and the Caltech Submillimeter Observatory (CSO), located at high, dry sites and equipped with sensitive receivers have become available. These facilities routinely observe lines at frequencies as high as 700 GHz and thus probe the densest, warmest parts of interstellar clouds.

In dense clouds, the excitation is dominated by collisions with molecular hydrogen, which is by far the most abundant species. However, in photon-dominated regions (PDRs), the electron abundance may be as high as 10^{-5} , and then collisions with electrons may become significant for some species. Additionally, in diffuse clouds and in the outer layers of PDRs atomic hydrogen can be an important collision partner.

In this paper we describe the results of statistical equilibrium calculations including spontaneous and stimulated radiative processes and collisional (de)excitation, focussing on the higher excitation lines. The radiative transfer is approximated through the mean escape probability method, but the lines are mostly assumed to be optically thin. This chapter will generally follow the notation used in Rybicki & Lightman (1979), Chapter 1.

2. Energy level structure

Linear molecules with a $^1\Sigma$ ground state have a very simple rotational energy level structure, and hence a simple spectrum, consisting of (almost) equally spaced lines, since $E_J = BJ(J+1)$ to first order and therefore $\Delta E = E_{J+1} - E_J = 2B(J+1)$, where J is the rotational quantum number and B the rotational constant; B is related to the structure of the molecule through

$$B = (2I_b)^{-1} = (2 \sum_i m_i r_{bi}^2)^{-1} \quad (1)$$

where m_i is the mass of the atom i and r_{bi} the distance between this atom and the center of mass. In some cases, this simple picture can be complicated by hyperfine structure, like in the case of HCN . Often the different hyperfine components are so close together,

that they can be considered as one line for the purpose of the excitation calculations. Although this approximation is not fully valid in the case of the lowest transitions of HCN, we will apply it in this chapter. Also, in the case of a $^2\Sigma$ ground state, e.g. CN and C₂H, or a $^3\Sigma$ ground state, e.g. SO, the rotational energy levels are split by the spin-rotation interaction.

Non-linear molecules like H₂CO, H₂CS, C₃H₂ and CH₃CN have a more complex energy level structure. In such a molecule, rotation around different axes of inertia involves different amounts of energy, determined by the three rotation constants A , B and C , where $A \geq B \geq C$. To describe the energy levels additional quantum numbers are needed than just the overall rotation quantum number J . The molecule is characterized by the quantity

$$\kappa = \frac{(C - B) - (B - A)}{(C - B) + (B - A)} \quad (2)$$

which is equal to -1 for *prolate* and $+1$ for *oblate* molecules. For purely prolate molecules, such as NH₃, the rotational energy levels are given to first order by

$$E_{\text{rot}} = BJ(J + 1) + (A - B)K^2 \quad (3)$$

where K is the prolate quantum number, and transitions are subject to the selection rules $\Delta J = \pm 1$, $\Delta K = 0$. A similar description can be made for purely oblate molecules, like benzene, where $(C - B)$ replaces $(A - B)$ in the expression for E_{rot} . Molecules with $\kappa \gtrsim -1$ can be treated as near-prolate, and those with $\kappa \lesssim 1$ as near-oblate. In these cases, K_p and K_o are defined as the K quantum number the level would have in the limiting prolate and oblate cases respectively, and the level is denoted by $J_{K_p K_o}$. The selection rules are not strict in these cases, but are usually obeyed. They are $\Delta J = 0, \pm 1$ and for near prolate species: $\Delta K_p = 0$, $\Delta K_o = \pm 1$ and vice versa for near oblate molecules.

A further complication arises when the molecule occurs in ortho and para varieties, due to the presence of two or more equivalent groups with non-zero nuclear spin, which are usually hydrogen atoms. Transitions between the ortho- and para states do not normally occur, not even through inelastic collisions. Only the exchange of H or H⁺ in reactive collisions can transfer the molecule from one state to the other. Such collisions essentially involve the exchange of one of the equivalent H atoms with an H atom from the collision partner, which is usually an ion, because ion-molecule reactions are fast under interstellar conditions, e.g.



The importance of such reactive collisions will be studied in this paper for H₂CO. Alternatively, one may ignore these transitions and assume that the ortho/para ratio is at its equilibrium value.

As an example, the energy levels of H₂CO are shown in Fig. 2. H₂CO is an excellent example of a near prolate molecule, in which the $\Delta K_p = 0$ rule is obeyed among the lower levels. Thus, the H₂CO levels can be arranged in ladders according to K_p . Collisions can transfer molecules between ladders, but radiative transitions can only occur within one ladder. Levels with even values of K_p belong to the para variety; those with odd values of K_p belong to ortho-formaldehyde.

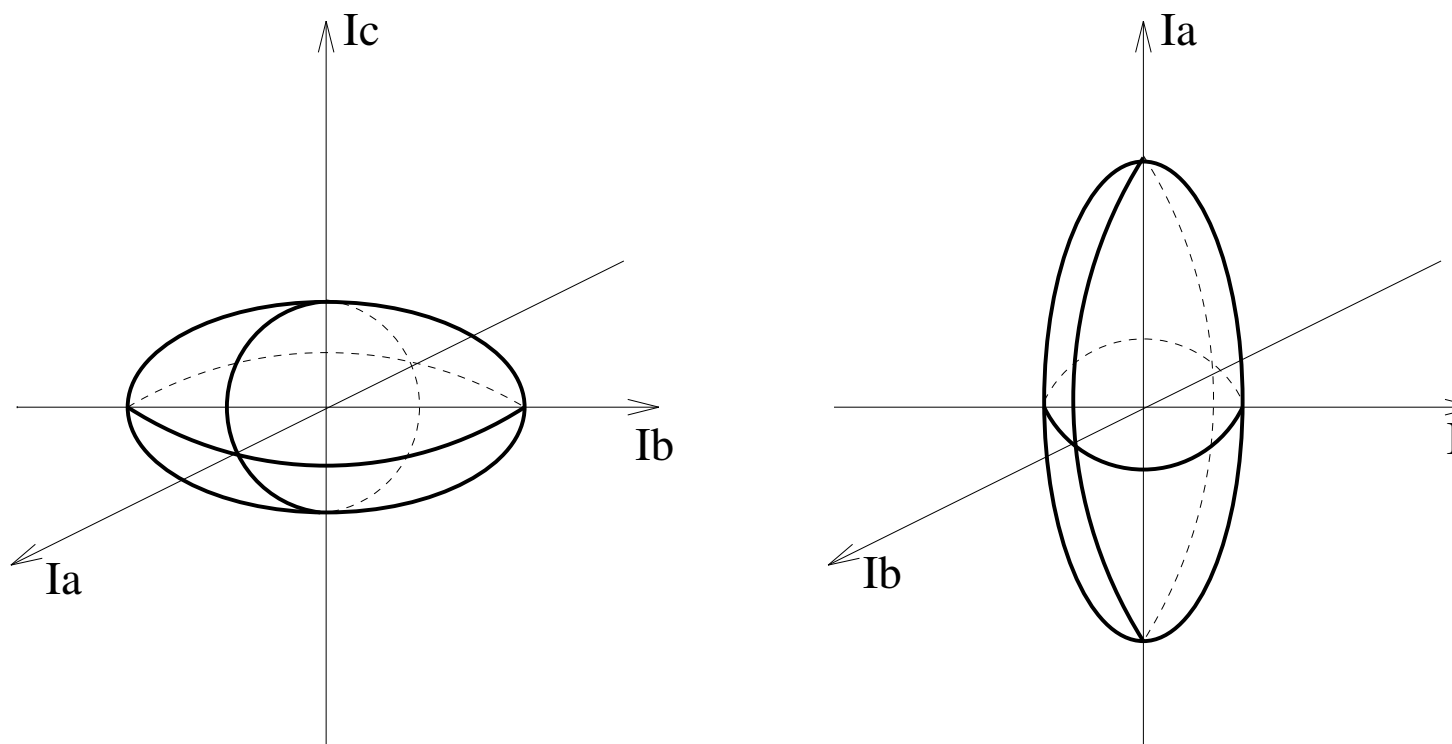


Figure 1. Principal rotation axes for an oblate symmetric top (left) and a prolate symmetric top (right).

Missing

Figure 2. Energy level diagram for H_2CO . Each J_{K_p} level with $K_p > 0$ is split into two levels because of the small departure from the pure prolate case. To convert the energy scale into K, multiply by 1.438768.

3. Level populations

The excited energy levels of a molecule can be populated by collisions and radiation. Collisions between molecules (or atoms) can both excite and de-excite a molecule. The collision rates depend on the partner involved in the collision. In most cases it is sufficient to take the most abundant collision partners into account, being H_2 and electrons. Radiation can excite a molecule through absorption and also de-excite it by stimulated and spontaneous emission. The latter process is independent of the external conditions. In some cases the excitation can be coupled to the chemistry, when a molecule is formed in an excited state and then radiates away the formation energy on a timescale that is long compared with time scales for competing processes. This will not be treated in this paper, except for the H exchange collisions for ortho/para interchange, as mentioned before in the case of H_2CO .

For a two-level system with levels labeled 1 and 2, the statistical equilibrium equations are

$$\begin{aligned}\frac{dn_1}{dt} &= -n_1(B_{12}\bar{J} + C_{12}) + n_2(A_{21} + B_{21}\bar{J} + C_{21}) \\ \frac{dn_2}{dt} &= n_1(B_{12}\bar{J} + C_{12}) - n_2(A_{21} + B_{21}\bar{J} + C_{21})\end{aligned}\tag{5}$$

where \bar{J} is the intensity of the radiation field averaged over all directions and integrated over the line profile. A_{ij} and B_{ij} are the Einstein A and B coefficients and C_{ij} is the collision rate between the two levels. This rate is equal to the collision partner density n_{col} times the velocity-integrated cross section or rate coefficient K_{ij} (in $\text{cm}^3 \text{s}^{-1}$):

$$\begin{aligned}K_{ij} &= \int \sigma_{ij} v p_{T_{\text{kin}}}(v) dv \\ C_{ij} &= n_{\text{col}} K_{ij}\end{aligned}\tag{6}$$

in which $p_{T_{\text{kin}}}(v)$ is the velocity distribution of the gas, which can be taken to be a Boltzmann distribution. Often the only important collision partner is H_2 ; in that case, the collision partner density is equal to the total (molecular) density: $n_{\text{col}} = n$.

The Einstein coefficients are given by

$$g_1 B_{12} = g_2 B_{21}\tag{7}$$

$$A_{21} = \frac{2h\nu^3}{c^2} B_{21}\tag{8}$$

where ν is the frequency of the transition, g_i is the statistical weight of level i and h and c are the Planck constant and the speed of light respectively. The Einstein A coefficient is related to the dipole moment of the molecule μ through

$$A_{21} = \frac{64\pi^4 \nu^3 \mu^2}{3c^3 h} \mathcal{S}_{21}\tag{9}$$

where \mathcal{S}_{21} is the transition strength. The upward and downward collisional rate coefficients are related through the principle of detailed balance:

$$K_{12} = K_{21} \frac{g_2}{g_1} e^{-h\nu/kT_{\text{kin}}}\tag{10}$$

In order to determine whether a molecule in the excited state will be more likely to decay to the ground state through emission of a photon or through a collisional de-excitation, one has to compare the density in the medium with the so-called critical density, which is the density at which the downward collisional processes equal the downward radiative processes. A molecule decays radiatively if the timescale for this process is smaller than the timescale for collisional de-excitation:

$$\frac{1}{A_{21}} \ll \frac{1}{C_{21}} \quad . \quad (11)$$

Since $C_{21} = nK_{21}$, we can write this relation as

$$n \ll n_{\text{crit}} \equiv \frac{A_{21}}{K_{21}} \quad . \quad (12)$$

This equation only holds in the optically thin limit. If the transition becomes optically thick, the critical density is lowered by $1/\tau$, since part of the emitted photons are re-absorbed, with no net effect on the level populations. Here τ is the optical depth of the line. Note also that higher frequency transitions have higher critical densities, since $A_{21} \propto \nu^3$.

This treatment can readily be extended to systems involving more than two energy levels. In that case, the statistical equilibrium equations become summations over upward and downward transitions. The definition of the critical density for a given transition becomes the ratio of the Einstein A coefficient for the transition, divided by the sum of all collisional transitions out of the upper level:

$$n_{\text{crit}} = \frac{A_{\text{ul}}}{\sum_i K_{\text{ui}}} \quad . \quad (13)$$

The critical densities listed in Table 2 are calculated using this equation.

4. Radiative transfer

The radiation field enters into Eq. 5 in the form of \bar{J} , which is the radiation field integrated over the line profile of the transition, averaged over all directions. \bar{J} is related to I_ν , the specific intensity at frequency ν . This quantity is defined as the radiation energy flowing through a surface per unit time per steradian in a specific frequency range, so

$$I_\nu = \frac{dE}{d\nu dA dt d\Omega \cos \theta} \quad . \quad (14)$$

I_ν is constant along a ray as long as the ray travels through a medium that neither absorbs nor emits at frequency ν , so that I_ν is independent of the distance to the source. This makes it the best suited quantity to formulate the radiative transfer equations.

In a medium that absorbs or emits radiation, I_ν is no longer constant. It decreases due to absorption, characterized by the absorption coefficient $\alpha_\nu(\vec{r})$, the fraction of the incident radiation that is absorbed in the volume element, and it increases due to emission, described by the emission coefficient $j_\nu(\vec{r})$. Note that stimulated emission is

included in $\alpha_\nu(\vec{r})$ as a negative contribution. The radiative transfer equation can be written as:

$$\frac{dI_\nu}{ds} = -\alpha_\nu(\vec{r})I_\nu + j_\nu(\vec{r}) \quad . \quad (15)$$

Both the absorption and emission coefficient may depend on position \vec{r} .

This equation can be rewritten in terms of the optical depth, which is at a point s along the ray defined as

$$\tau_\nu(s) = \int_0^s \alpha(s') ds' \quad . \quad (16)$$

With this definition, the equation for radiative transfer becomes

$$\frac{dI_\nu}{d\tau_\nu} = -I_\nu + S_\nu(\tau_\nu) \quad (17)$$

where the source function $S_\nu(\tau_\nu)$ is defined as the ratio of the emission and absorption coefficients. The formal solution to this differential equation is

$$I_\nu(\tau_\nu) = I_\nu(0)e^{-\tau_\nu} + \int_0^{\tau_\nu} S_\nu(\tau'_\nu)e^{-(\tau_\nu-\tau'_\nu)} d\tau'_\nu \quad (18)$$

in which the first term stands for the fraction of the background radiation that is able to get through the medium, and the second term is the radiation emitted by the medium that manages to get out.

The total intensity independent of direction is obtained by integrating over all solid angles:

$$J_\nu = \frac{1}{4\pi} \int I_\nu d\Omega \quad (19)$$

and \bar{J} is this intensity integrated over the line profile $\phi(\nu)$. This becomes important when the line gets optically thick in the center, but not yet in the wings, since in that case the radiative transfer is different in different parts of the profile. However, in this paper we will ignore these effects and look only at the intensity (and optical depth) at the line center, so basically the line is treated as a rectangular profile with width ΔV .

The emission- and absorption coefficients can be expressed in terms of the Einstein coefficients:

$$\begin{aligned} j_\nu &= \frac{h\nu}{4\pi} n_2 A_{21} \phi(\nu) \\ \alpha_\nu &= \frac{h\nu}{4\pi} (n_1 B_{12} - n_2 B_{21}) \phi(\nu) \end{aligned} \quad . \quad (20)$$

Therefore, the source function can be written as

$$S_\nu = \frac{n_2 A_{21}}{n_1 B_{12} - n_2 B_{21}} \quad . \quad (21)$$

In the case of thermodynamic equilibrium, the level populations will have a Boltzmann distribution:

$$\frac{n_2}{n_1} = \frac{g_2}{g_1} e^{-h\nu_0/kT_{\text{kin}}} \quad (22)$$

where ν_0 is the frequency at line center. In general, the interstellar medium is not in thermodynamic equilibrium, but it is often useful to define an excitation temperature T_{ex} through

$$\frac{n_2}{n_1} = \frac{g_2}{g_1} e^{-h\nu_0/kT_{\text{ex}}} \quad (23)$$

i.e. T_{ex} is the temperature at which a Boltzmann distribution would yield the same relative populations in levels 1 and 2. Note that in a multi-level system every transition may have a different excitation temperature. Alternatively, the excitation temperature can be defined by

$$S_\nu = B_\nu(T_{\text{ex}}) \quad (24)$$

where $B_\nu(T)$ is the Planck function, or the source function of a black body at temperature T :

$$B_\nu(T) = \frac{2h\nu^3/c^2}{e^{h\nu/kT} - 1} \quad (25)$$

5. Escape probability

In order to decouple the equations for the level populations and the radiative transfer (Eqs. 5 and 18), one needs to make some assumptions. One way is the so-called “escape probability method”, in which the probability β indicates the fraction of the photons that manage to escape from the cloud. The intensity inside the cloud then becomes $\bar{J} = S(1 - \beta)$, where S is the source function integrated over the line profile. Substituting for \bar{J} in Eq. 5 gives

$$\frac{dn_2}{dt} = n_1 C_{12} - n_2 C_{21} - \beta n_2 A_{21} \quad (26)$$

which does not contain the radiation field any more, so that the level populations can be solved separately from the radiation field.

The next step is to find a reasonable expression for β . Obviously, this expression will depend on the optical depth of the medium and on the geometry, but not on the radiation field. For $\tau = 0$, the escape probability should be unity, and it should decrease with increasing τ . Here we will not consider the case $\tau < 0$, which is appropriate for masers.

A derivation of the expression for a homogeneous spherical nebula can be found in Osterbrock (1989), resulting in:

$$\beta = \frac{3}{2\tau} \left(1 - \frac{2}{\tau^2} + \left(\frac{2}{\tau} + \frac{2}{\tau^2} \right) e^{-\tau} \right) \quad (27)$$

Note that in this equation, τ is the optical diameter of the cloud, whereas in Osterbrock (1989) it is the optical radius. This is done for consistency with other geometries, where τ also indicates the total optical depth through the medium. In a similar manner, one can derive an escape probability for a plane-parallel homogeneous slab:

$$\beta = \frac{(1 - e^{-3\tau})}{3\tau} \quad (28)$$

and in the so called Sobolev- or Large Velocity Gradient approximation (Sobolev 1960; de Jong et al. 1980; Habing 1988):

$$\beta = \frac{(1 - e^{-\tau})}{\tau} \quad . \quad (29)$$

In general, the differences between these geometries are small, as can be seen in Fig. 3. In this work, the escape probability is computed using Eq. 27.

Missing

Figure 3. *Escape probability β as a function of optical depth for various geometries. Solid line: spherical geometry; long dashes: plane parallel slab; short dashes: large velocity gradient.*

6. Background radiation field

The ambient radiation field is of great importance in the analysis of the excitation balance of atoms or molecules, especially those parts of the spectrum where absorption of a photon leads to a significant alteration of the level populations. In many molecules, excitation into an electronically or vibrationally excited state does not lead to emission in the pure rotational lines that we are interested in here. Moreover, in many cases the redistribution among the rotational levels in the ground state is much faster than the typical time scale for excitation into a higher vibrational or electronic state. In these cases, only the far-infrared and (sub)millimeter spectrum have to be taken into account. The spectrum in the millimeter regime is usually dominated by the cosmic background 2.73 K black body radiation field, which peaks at 1.871 mm. For “heavy rotors”, such as CO, CS, HCN, HCO⁺ and H₂CO this component of the radiation field therefore controls the radiative excitation, thus removing the need for knowledge of the specific radiation field for the cloud altogether.

For lighter hydrides, such as OH, H₂O, H₃O⁺, NH₂ and NH₃, the far- and mid-infrared radiation field is important, since these molecules have widely spaced rotational energy levels (cf. Eq. 1). The most important contributions in this wavelength regime are from dust emission, especially in circumstellar material or in star-forming regions. The dust emission is characterized by a dust temperature T_d , a dust opacity τ_d and a geometrical dilution factor η_d which indicates the fraction of the dust emission actually seen by the molecules. The background radiation field seen by the molecules inside the cloud is then given by

$$I_\nu^{\text{background,int}} = B_\nu(T_{\text{CB}}) + \eta_d B_\nu(T_d)(1 - e^{-\tau_d}) \quad (30)$$

whereas the background seen by the observer is

$$I_\nu^{\text{background}} = B_\nu(T_{\text{CB}}) + B_\nu(T_d)(1 - e^{-\tau_d}) \quad . \quad (31)$$

In most of the calculations presented in this chapter the cosmic background is used as the only contribution to the radiation field. A few examples are shown where infrared dust emission is included in the excitation of light hydrides.

7. Computing line intensities

Once the level populations are known the intensity of the lines can be calculated. The level populations are often expressed in terms of x_i , which are the normalized counterparts of the n_i used in previous sections: $x_i = n_i / \sum_j n_j$.

First, the optical depth is computed. In this paper we will only concern ourselves with the optical depth at line center (τ_0), or equivalently, assume that the line has a rectangular shape with width $\Delta\nu = \nu_0 \frac{\Delta V}{c}$:

$$\begin{cases} \phi(\nu) = 1 & \text{if } |\nu - \nu_0| < \frac{1}{2}\Delta\nu \\ \phi(\nu) = 0 & \text{otherwise} \end{cases} \quad (32)$$

Now τ_0 is related to the level populations by

$$\tau_0 = \frac{A_{21}c^3}{8\pi\nu^3} \frac{N(\text{mol})}{\Delta V} (x_1 \frac{g_2}{g_1} - x_2) \quad . \quad (33)$$

Thus, the optical depth — and therefore the line intensity as well — only depend on the ratio of the total column density of the molecule, $N(\text{mol})$, and the line width. Once τ_0 is computed through an iterative scheme, the observed line intensity in excess of the background can be calculated according to

$$\Delta I_\nu = I_\nu^{\text{total}} - I_\nu^{\text{background}} = (B_\nu(T_{\text{ex}}) - I_\nu^{\text{background}})(1 - e^{-\tau_0}) \quad (34)$$

The Rayleigh-Jeans equivalent temperature T_R , which is the quantity that is directly comparable to the observations, is given by:

$$T_R = \frac{c^2}{2k\nu^2} \Delta I_\nu \quad . \quad (35)$$

In the case of an optically thick line, the radiation temperature will become equal to the excitation temperature, and if the line is thermalized, this temperature will be equal to the kinetic temperature in the frequency regime where the Rayleigh-Jeans approximation is valid. Note, however, that in the submillimeter regime this approximation usually does not hold. Even so, optically thick, thermalized lines, such as the lines of ^{12}CO , can be used as temperature tracers (see Chapter 3).

8. Collisional rate coefficients

The largest uncertainty in the process of analyzing the molecular excitation usually stems from the adopted rate coefficients for collisions with molecular hydrogen and free electrons.

Rates for collisions with H_2 have only been measured for a few species, so that virtually all data have been derived from theory. A detailed account of the various theoretical methods and their associated uncertainties is given by Green (1975b) and Flower (1990). For some systems, such as CO-H_2 at low temperatures, the rate coefficients are thought to be accurate to better than 20%. However, for larger molecules, especially those with open shells, the absolute results may be uncertain by a factor of a few. The relative rate coefficients for transitions within the same molecule are generally more reliable. References to the adopted collision rates in this work can be found in Table 1. In some cases, we have scaled the rate coefficients for a molecule from those that were published for another, similar molecule. The collision rates for HCS^+ and H_2CS were derived from those of HCO^+ and H_2CO respectively, only scaled for the difference in reduced mass. Similarly, the rates for C_2H were assumed to be equal to those of HCN . Also, for some molecules only rate coefficients for collisions with helium are available in the literature. These can be used for collisions with molecular hydrogen, after scaling for the mass of the collision partner, since molecular hydrogen in its ground $J = 0$ state is a “structureless particle”, much like the helium atom. Collisions with H_2 $J = 1$ or higher have not explicitly been taken into account in this work, due to lack of reliable rate coefficients in general.

Collisions with electrons have only been included for a few specific molecules, where they have a significant contribution to the excitation. Usually, collisional excitation by electrons starts to become comparable to the effect of hydrogen when the electron fraction is 10^{-5} or higher, which only occurs in the outer layers of photon dominated regions (PDRs), where not many molecules reside. Rates for collisions with electrons were computed according to the approximation of Dickinson & Flower (1981) and Dickinson et al. (1977).

Whereas radiative transitions follow selection rules $\Delta J = \pm 1$ (or $\Delta J = 0$ when $\Delta K \neq 0$), collisional transitions are possible for higher values of ΔJ . For collisions with H_2 , the $\Delta J = \pm 2$ collisional rate coefficients are generally substantial. Collisions with electrons favor $\Delta J = \pm 1$. Moreover, symmetric top molecules such as H_2CO have no allowed radiative transitions between different K_p -ladders. The relative population of these ladders is therefore dominated by collisions only.

Table 1. Collisional rate coefficients

Species	Collision partner	Reference
CO	H ₂	Schinke et al. (1985) ($J \leq 4$); Flower & Launay (1985) ($J > 4$)
CS	H ₂	Green (priv. comm., cf. Turner et al. 1992)
CN	H ₂	from CS rates (Green & Chapman 1978; see Black & van Dishoeck 1991)
HCO ⁺	H ₂	Green (1975a), Monteiro (1985)
HCN	He	Green & Thaddeus (1974)
(hfs)		Monteiro & Stutzki (1986)
H ₂ CO	H ₂	Green (1991)
C ₂ H	He	from HCN rates (Green & Thaddeus 1974)
C ₃ H ₂	He	Green et al. (1987)
N ₂ H ⁺	H ₂	Green (1975a)
CH ₃ CN	H ₂	Green (1986)
HC ₃ N	H ₂	Green & Chapman (1978)
HDO	He	Green et al. (1989)
H ₃ O ⁺	H ₂	Offer & Van Hemert (1992)
SiO	H ₂	Green (priv. comm., cf. Turner et al. 1992)
SO	H ₂	Green (1995)
OCS	H ₂	Green & Chapman (1978)
HCS ⁺	H ₂	from HCO ⁺ rates (Monteiro 1985)
H ₂ CS	H ₂	from H ₂ CO (Green 1991)

9. Calculations

A computer program incorporating the parameters discussed in the previous section was written originally by J.H. Black, and modified to suit the needs of this research. It requires for each molecule the molecular energy levels, Einstein A-coefficients for all radiatively allowed transitions, and statistical weights. Next, it needs the downward collisional rate coefficients for one or two collision partners, which are usually H₂ and free electrons. Different sets of collisional rate coefficients can be used for different temperatures, and the program interpolates these for the required conditions. The upward rate coefficients are then computed through detailed balance (Eq. 10).

The main input parameters are the temperature, density of the collision partner(s), column density of the molecule in question and the width of the line. In fact, the results only depend on the ratio of column density and profile width, as can be seen from Eq. 33. The background radiation field can also be specified, as discussed before. The program can handle black body radiation, dust and free-free emission, or a power-law spectrum ranging from radio to visible wavelengths, but in this work, only the cosmic background will be considered, and dust emission for a few light hydrides.

In the next section we will show the results for the ratio of two lines of the same molecule as a function of H₂ density and kinetic temperature. In the optically thin case, the line ratio does not depend on $N(\text{mol})/\Delta V$, since all lines are proportional to this quantity. Therefore, such a line ratio only depends on density, temperature and

the radiation field. It may also depend on the presence of a second collision partner, which is considered in §10.3. The background radiation field is kept fixed in each of these model runs at $T_{\text{CB}} = 2.73 \text{ K}$.

In this chapter, we investigate the molecular excitation in the range $1 \times 10^3 \text{ cm}^{-3} < n(\text{H}_2) < 1 \times 10^8 \text{ cm}^{-3}$ and $20 \text{ K} < T_{\text{kin}} < 200 \text{ K}$. In all cases $N(\text{mol})/\Delta V = 1 \times 10^{12} \text{ cm}^{-2} \text{ km}^{-1} \text{ s}$ is used, which ensures that the lines are optically thin, and $X(\text{e}) = 0$. At temperatures lower than 20 K, the lowest lines become highly optically thick, even for such a low column density, since there will be virtually no population in the upper levels. The data files for all species contain sufficiently high energy levels to extend the calculations up to 200 K. The focus will be on lines that are observable from the ground in the atmospheric frequency windows up to 500 GHz.

Figure 4 shows a few synthetic spectra calculated for characteristic temperatures and densities. This figure mainly illustrates at which frequency one expects the strongest lines for a given temperature and density. It is seen that the strongest lines generally occur between 100 and 400 GHz. Note that the lowest frequency lines of H_2CO at centimeter wavelengths are predicted to be in absorption at low densities.

10. Results and discussion

The results of the calculations are displayed in Figures 7 to 22 at the end of this Chapter. These figures show contours of equal line ratio, as functions of collision partner density and kinetic temperature. In Fig. 7 to 17, the collision partner is molecular hydrogen, and thus the horizontal axis denotes the total molecular density.

In order to give some feeling for the diagnostic value of such plots, the observed line ratios for the young stellar object IRAS 16293 –2422 (Blake et al. 1994; Van Dishoeck et al. 1995) are included in the figures as shaded areas. The interpretation of these observational data is postponed to §11 of this chapter.

As can be seen from the figures, some line ratios are mainly sensitive to density, whereas others are sensitive to temperature. The density dependence follows from the equation for the critical density (Eq. 12). Lines with a small Einstein A coefficient are only sensitive to density in the low density regime. This is especially the case for molecules with a small dipole moment, such as CO. Other lines are sensitive to density over the whole range considered in this chapter. Since $A_{ul} \propto \nu^3$, this means that higher frequency transitions are sensitive to higher densities. A list of critical densities for all the transitions used in this work is presented in Table 2.

For a simple, linear molecule like CS or HCO^+ , the difference in frequency between two adjacent lines causes a big difference in the critical density, but the difference in excitation energy causes only a slight difference in temperature dependency, which explains the shape of the curves seen, e.g., in the CS $2 \rightarrow 1 / 5 \rightarrow 4$ ratio in Fig. 7d: The ratio decreases for higher density, because the $5 \rightarrow 4$ line becomes stronger with increasing density, and the $2 \rightarrow 1$ line does not. At constant density, the ratio is lower at higher temperatures, since such temperatures favor the transition that lies higher in energy. The temperature dependency is stronger below the critical densities of the transitions, and almost vanishes once the density is above this value. This is also reflected in the change in slope of the contours below $T = 30 \text{ K}$, since at lower temperatures, the excitation energy for the $J = 5$ level of CS (35 K) is not yet reached. These same features are seen in other diagrams, such as that for HCO^+ $1 \rightarrow 0 / 4 \rightarrow 3$

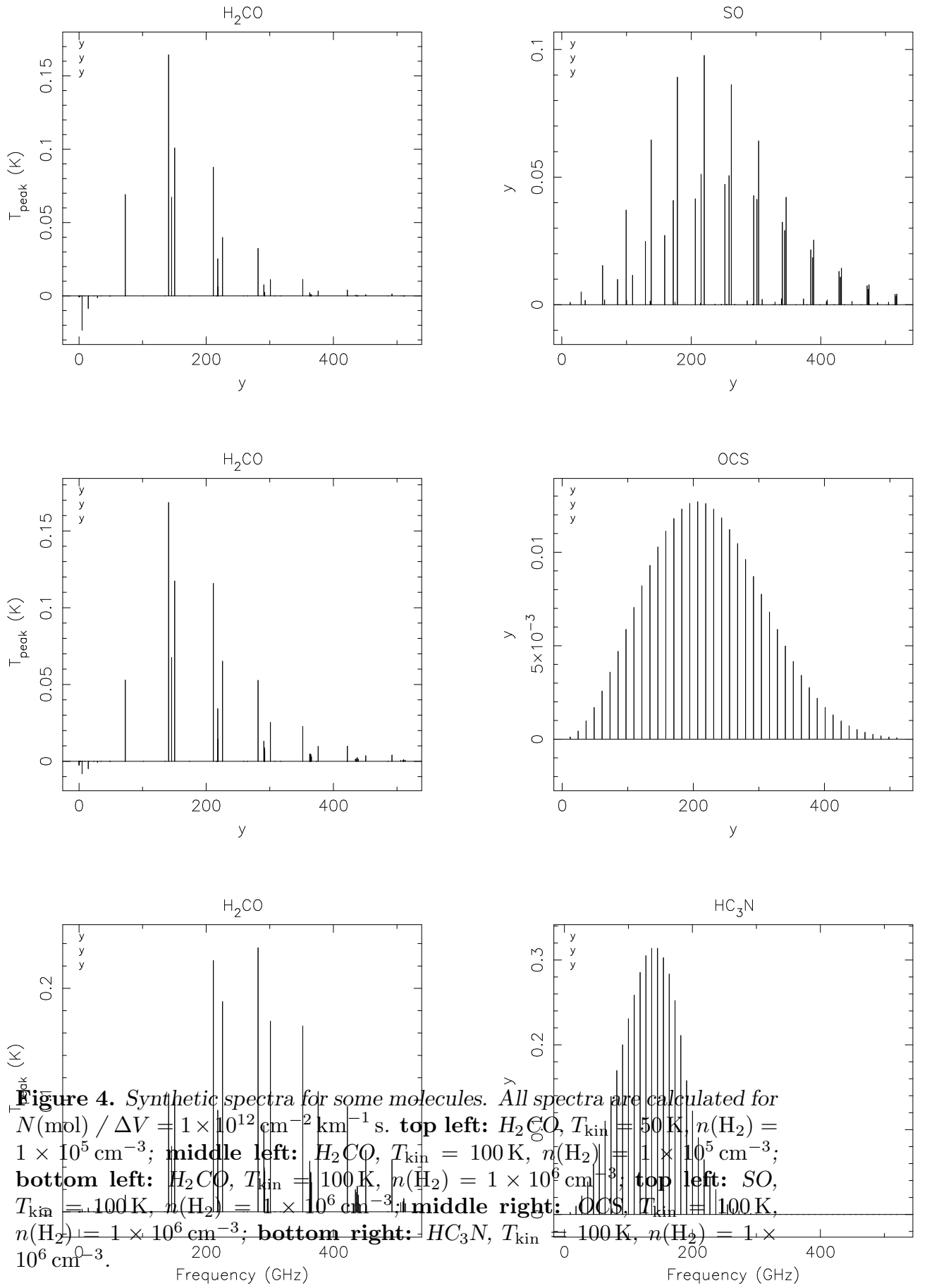


Table 2. Critical densities for the transitions

Molecule	Transition	Frequency (GHz)	E_{upper} (K)	n_{crit}^a (cm^{-3})
CO	$1 \rightarrow 0$	115.271	5.5	4.1 (2)
	$2 \rightarrow 1$	230.538	16.6	2.7 (3)
	$3 \rightarrow 2$	345.796	33.2	8.4 (3)
	$4 \rightarrow 3$	461.041	55.3	1.9 (4)
	$7 \rightarrow 6$	806.652	154.9	9.4 (4)
CS	$2 \rightarrow 1$	97.981	7.1	8.0 (4)
	$3 \rightarrow 2$	146.969	14.1	2.5 (5)
	$5 \rightarrow 4$	244.936	35.3	1.1 (6)
	$7 \rightarrow 6$	342.883	65.8	2.9 (6)
	$10 \rightarrow 9$	489.751	129.3	8.1 (6)
CN	$2 \frac{5}{2} \rightarrow 1 \frac{3}{2}$	226.874	16.3	1.4 (6)
	$3 \frac{7}{2} \rightarrow 2 \frac{5}{2}$	340.248	32.7	6.0 (6)
HCN	$1 \rightarrow 0$	88.632	4.3	2.3 (5)
	$3 \rightarrow 2$	265.886	25.5	4.1 (6)
	$4 \rightarrow 3$	354.506	42.5	8.5 (6)
HCO ⁺	$1 \rightarrow 0$	89.189	4.3	3.4 (4)
	$3 \rightarrow 2$	267.558	25.7	7.8 (5)
	$4 \rightarrow 3$	356.734	42.8	1.8 (6)
H ₂ CO (para)	$2_{02} \rightarrow 1_{01}$	145.603	10.5	1.6 (5)
	$3_{03} \rightarrow 2_{02}$	218.222	21.0	4.7 (5)
	$5_{05} \rightarrow 4_{04}$	362.736	52.3	1.9 (6)
	$3_{22} \rightarrow 2_{21}$	218.476	68.1	2.3 (5)
	$5_{23} \rightarrow 4_{22}$	365.363	99.7	1.6 (6)
H ₂ CO (ortho)	$2_{12} \rightarrow 1_{11}$	140.840	21.9	1.0 (5)
	$2_{11} \rightarrow 1_{10}$	150.498	22.6	1.2 (5)
	$3_{12} \rightarrow 2_{11}$	225.698	33.5	4.5 (5)
	$5_{15} \rightarrow 4_{14}$	351.769	62.5	1.7 (6)
	$5_{33} \rightarrow 4_{32}$	364.340	158.4	1.3 (6)
SiO	$2 \rightarrow 1$	86.847	6.3	1.3 (5)
	$5 \rightarrow 4$	217.105	31.3	1.7 (6)
	$6 \rightarrow 5$	260.518	43.8	2.9 (6)
	$8 \rightarrow 7$	347.331	75.0	6.4 (6)
SO	$2_2 \rightarrow 1_1$	86.094	19.3	8.5 (4)
	$5_6 \rightarrow 4_5$	219.949	35.0	5.6 (5)
	$5_5 \rightarrow 4_4$	215.220	44.1	4.8 (5)
	$6_5 \rightarrow 5_4$	251.826	50.7	6.2 (5)
	$6_6 \rightarrow 5_5$	258.256	56.5	7.9 (5)
	$8_9 \rightarrow 7_8$	346.528	78.8	2.0 (6)
	$8_7 \rightarrow 7_6$	340.714	81.2	1.5 (6)
	$8_8 \rightarrow 7_7$	344.310	87.5	1.8 (6)
OCS	$18 \rightarrow 17$	218.903	99.8	5.1 (4)
	$20 \rightarrow 19$	243.218	122.6	7.0 (4)
	$21 \rightarrow 20$	255.374	134.8	8.1 (4)
	$22 \rightarrow 21$	267.530	147.7	9.4 (4)
	$28 \rightarrow 27$	340.449	237.0	1.9 (5)

^a Calculated for $T_{\text{kin}} = 100$ K in the optically thin limit.

Table 2. (continued)

Molecule	Transition	Frequency (GHz)	E_{upper} (K)	n_{crit}^a (cm^{-3})
HCS ⁺	2 \rightarrow 1	85.348	6.1	1.5 (4)
	5 \rightarrow 4	213.361	30.7	3.2 (5)
	6 \rightarrow 5	256.027	43.0	6.5 (5)
	8 \rightarrow 7	341.351	73.7	2.2 (6)
H ₂ CS (ortho)	7 ₁₇ \rightarrow 6 ₁₆	236.727	58.6	2.6 (5)
	7 ₃₅ \rightarrow 6 ₃₄	240.393	164.6	2.3 (5)
	10 _{1,10} \rightarrow 9 ₁₉	338.081	102.4	8.9 (5)
	10 ₃₈ \rightarrow 9 ₃₇	343.408	209.1	1.0 (6)
H ₂ CS (para)	7 ₀₇ \rightarrow 6 ₀₆	240.266	46.1	2.7 (5)
	10 _{0,10} \rightarrow 9 ₀₉	342.944	90.6	9.4 (5)
	7 ₂₆ \rightarrow 6 ₂₅	240.382	98.8	2.6 (5)
	10 ₂₉ \rightarrow 9 ₂₈	343.319	143.3	9.3 (5)
CH ₃ CN (ortho)	7 ₄₄ \rightarrow 6 ₄₃	240.331	256.6	3.9 (5)
	12 ₀ \rightarrow 11 ₀	220.747	68.9	1.4 (6)
	12 ₃ \rightarrow 11 ₃	220.709	132.8	1.3 (6)
	13 ₀ \rightarrow 12 ₀	239.138	80.3	1.7 (6)
CH ₃ CN (para)	14 ₀ \rightarrow 13 ₀	257.527	92.7	2.2 (6)
	12 ₁ \rightarrow 11 ₁	220.743	76.0	1.4 (6)
	12 ₂ \rightarrow 11 ₂	220.730	97.3	1.4 (6)
	12 ₄ \rightarrow 11 ₄	220.679	182.5	1.7 (6)
HC ₃ N	10 \rightarrow 9	90.979	24.0	9.6 (4)
	16 \rightarrow 15	145.560	59.4	4.2 (5)
	24 \rightarrow 23	218.325	131.0	1.6 (6)
	25 \rightarrow 24	227.419	141.9	1.8 (6)
	27 \rightarrow 26	245.606	165.1	2.3 (6)
	28 \rightarrow 27	254.700	177.3	2.6 (6)
N ₂ H ⁺	1 \rightarrow 0	93.173	4.5	7.2 (4)
	4 \rightarrow 3	372.673	44.7	4.4 (6)
	5 \rightarrow 4	465.825	67.1	9.2 (6)
C ₂ H	3 ₄ \rightarrow 2 ₃	262.004	25.1	2.1 (5)
	4 ₅ \rightarrow 3 ₄	349.338	41.9	5.3 (5)
C ₃ H ₂ (ortho)	3 ₃₀ \rightarrow 2 ₂₁	216.279	19.5	1.1 (6)
	4 ₃₂ \rightarrow 3 ₂₁	227.169	29.1	1.8 (6)
	5 ₂₃ \rightarrow 4 ₃₂	249.054	41.0	2.9 (6)
	5 ₃₂ \rightarrow 4 ₄₁	260.480	44.7	2.5 (6)
	5 ₅₀ \rightarrow 4 ₄₁	349.264	49.0	8.7 (6)
C ₃ H ₂ (para)	3 ₃₁ \rightarrow 2 ₀₂	261.832	19.0	1.2 (6)
	5 ₅₁ \rightarrow 4 ₄₀	338.204	48.8	8.4 (6)
HDO	1 ₀₁ \rightarrow 0 ₀₀	464.925	22.3	6.9 (6)
	2 ₁₁ \rightarrow 2 ₁₂	241.562	95.2	1.3 (8)
	3 ₁₂ \rightarrow 2 ₂₁	225.897	167.6	3.2 (8)
H ₃ O ⁺	1 ₁₀ \rightarrow 1 ₀₁	509.292	46.8	8.9 (7)
	3 ₀ ⁺ \rightarrow 2 ₀ ⁻	396.272	169.3	1.5 (6)
	1 ₁ ⁻ \rightarrow 2 ₁ ⁺	307.192	79.5	1.6 (8)
	3 ₂ ⁺ \rightarrow 2 ₂ ⁻	364.797	139.2	7.8 (5)

^a Calculated for $T_{\text{kin}} = 100$ K in the optically thin limit.

in Fig. 8b. It can be seen that these transitions have a lower critical density than the CS transitions in Fig. 7d.

When higher energy levels are considered, the picture changes, to the extent that a larger part of the diagram — the part with densities lower than the critical density — is dominated by temperature. Good examples of this are Fig. 7d and f (CS $5 \rightarrow 4$ / $7 \rightarrow 6$ and $7 \rightarrow 6$ / $10 \rightarrow 9$), because the $J = 7$ level lies at 66 K and $J = 10$ at 129 K. This, however, does not make these transitions good temperature tracers, since the absolute intensity of the lines is often very low in this regime. If the lines are observable at all, then often the signal-to-noise ratio is too low to make a useful temperature determination possible. For example, in the IC 63 nebula (Jansen et al. 1994; Chapter 3) — a cloud with $n(\text{H}_2) \approx 5 \times 10^4 \text{ cm}^{-3}$ and $T_{\text{kin}} \approx 50 \text{ K}$ — no detections were made of the CS $5 \rightarrow 4$ and higher- J transitions.

The shape of the CO plots can be explained in the same way as those of CS. The difference in appearance is caused by the difference in critical density between the two species, since CO has a very small dipole moment. This causes the contours to shift to lower densities, but the energy levels are comparable to those in e.g. HCO^+ , resulting in a similar temperature dependence.

It can also be seen from the figures that different line ratios from the same molecule trace different regimes in parameter space. This is even more apparent for bigger linear molecules, such as HC_3N . Such molecules have, due to their weight, a closely spaced energy ladder, and thus many observable transitions in a given atmospheric window. The $10 \rightarrow 9$ / $16 \rightarrow 15$ ratio, shown in Fig. 14b, is an useful density tracer in the range $1 \times 10^4 \lesssim n \lesssim 2 \times 10^5 \text{ cm}^{-3}$, whereas a ratio like $24 \rightarrow 23$ / $28 \rightarrow 27$ is sensitive to $5 \times 10^5 \lesssim n \lesssim 1 \times 10^7 \text{ cm}^{-3}$. Therefore, a molecule like HC_3N will be a very good density tracer — if observable.

The plots of the linear OCS molecule (Fig. 11) are an extreme case of the behavior seen in other molecules as well: at constant kinetic temperature, the line ratio first increases with increasing density, and after reaching a maximum, it drops off again. The part where the density is higher than the critical density is similar to the case of CS described above; the line ratio depends only on density in this regime. Starting at low density, the lowest excitation line increases faster in intensity than the higher excitation line, causing the line ratio to increase. This continues until the critical density for the higher- J line is reached, and from then on, the ratio drops down again. This effect is more important for OCS than for other species, since OCS has many closely spaced energy levels, so the ratio between a line in the 200 GHz window and one in the 300 GHz window involves two lines with a large difference in critical density. When one considers the ratio between two consecutive lines, like the $20 \rightarrow 19$ / $21 \rightarrow 20$ ratio in Fig. 11e, the pattern is more like that of CS.

A molecule for which collisional rate coefficients have only recently become available is SO (Green 1995). This molecule has a somewhat different energy level structure, due to its $^3\Sigma$ ground state. This causes a splitting of each of the rotational energy levels. Line ratios for the SO molecule are shown in Figure 13. In general, the line ratios are good density tracers and exhibit the same behavior as described previously for CS.

A molecule like H_2CO has a more complex energy level structure (see Fig. 2). As long as lines within one K_p ladder are considered, the structure is similar to CS and HCO^+ . Line ratios such as $3_{03} \rightarrow 2_{02}$ / $5_{05} \rightarrow 4_{04}$ and $3_{12} \rightarrow 2_{11}$ / $5_{15} \rightarrow 4_{14}$ are therefore

mainly sensitive to density, and only become temperature dependent when the density is below the critical densities of both transitions. These line ratios are shown in Fig. 9. In addition, H_2CO has, in different K_p ladders, multiple lines at about the same frequency — and therefore about the same critical density — but with very different excitation energies. The ratio between two of these lines will be mainly controlled by the temperature, as can be seen in Fig. 10. Actually, the fact that these lines are so close in frequency makes them very good observational probes as well, since both lines can often be observed in one frequency setting with the same receiver, hence eliminating calibration uncertainties. As seen from the figures, the H_2CO $3_{03} - 2_{02} / 3_{22} - 2_{21}$ ratio is probably the best probe for temperatures between 20 and 100 K, and ratios like $5_{15} - 4_{14} / 5_{33} - 4_{32}$ are good for higher temperatures. Figure 2 shows that each J_{K_p} level with $K_p > 0$ is split into two levels with different K_o . Therefore, transitions in these ladders come in pairs, but the two lines within such a pair show similar, if not identical, behavior. Thus, the plots concerning e.g. the $3_{22} \rightarrow 2_{21}$ transition, for example, can equally well be applied to the $3_{21} \rightarrow 2_{20}$ transition. The H_2CS molecule shows the same properties as H_2CO (see Fig. 12). Another good temperature tracer is the symmetric top molecule CH_3CN shown in Fig. 15. Transitions of this molecule occur in bands such as $12_K \rightarrow 11_K$. The lines within one band are close in frequency and critical density, but the different ladders lie at rather different energies. Ratios between lines within one band therefore depend only on temperature.

10.1. Effects of optical depth

All of the calculations shown in Fig. 7 to 17 are for a low column density of the molecule ($N(\text{mol}) = 1 \times 10^{12} \text{ cm}^{-2}$), so even the diagrams for CO involve the ratio of optically thin lines. Once a line becomes saturated, its intensity will stop increasing even if it is in the density and temperature regime below the critical density. If the other line involved in the line ratio is still thin, then the ratio will change in favor of the optically thin line.

Figure 18 shows the effect of optical depth on the calculated line ratios. This figure is for CO, with a column density of $1 \times 10^{17} \text{ cm}^{-2}$ and line width $\Delta V = 1 \text{ km s}^{-1}$. Also shown are the optical depths of the lines. If these figures are compared to the corresponding panels of Figure 7, it can be seen that the $2 \rightarrow 1 / 3 \rightarrow 2$ ratio at the same $(n(\text{H}_2), T_{\text{kin}})$ point is higher in the case of the high column density. This is due to the fact that the higher- J lines become more saturated with increasing density than the lower- J lines because the optical depth is proportional to ν^3 . Therefore, the $2 \rightarrow 1$ line is able to get stronger, whereas the $3 \rightarrow 2$ line is already saturated and cannot gain any more intensity. The same happens with the $4 \rightarrow 3 / 7 \rightarrow 6$ ratio at high densities. However, at lower densities, the intensity of the $7 \rightarrow 6$ line is very low, although it has optical depth greater than 1. This means that photons will be absorbed, but the density is too low to collisionally de-excite the molecules, so that the molecules will re-emit the photons.

10.2. *Effects of the far-infrared radiation field*

The main effect of a radiation field on the level population is through stimulated absorption, which is most effective in the (far-) infrared. Which molecules are sensitive to this pumping? In general, all molecules for which the lowest radiative transitions occur at (far-)infrared wavelengths.

One example is HDO, the deuterated isotope of water; its ground state transition ($1_{01} \rightarrow 0_{00}$) occurs at 464 GHz. Two other observable transitions are the $3_{12} \rightarrow 2_{21}$ at 225 GHz, and the $2_{11} \rightarrow 2_{12}$ at 241 GHz. The latter two lines turn out to be very sensitive to dust emission at infrared wavelengths, which is able to enhance the population in the upper levels through absorption in higher frequency rotational lines which connect with the ground state. Without this contribution to the radiation field, the $3_{12} \rightarrow 2_{21}$ line is several orders of magnitude weaker than the ground state line, and therefore impossible to detect (see Fig. 19, top left panel). Once there is sufficient infrared emission to populate the upper level, the line becomes of the same order as the ground state line. This is shown in Fig. 19 (top right panel), where the grid is parameterized by the color excess $E(B - V)$, which is a measure for the amount of dust, and the dust temperature T_{dust} . Since the dust dominates the excitation of the $3_{12} \rightarrow 2_{21}$ line, and hardly affects the $1_{01} \rightarrow 0_{00}$ transition, the ratio of these two lines becomes almost independent of the gas density and temperature, and thus this ratio may be used to determine the dust properties. A similar situation occurs for the $2_{11} \rightarrow 2_{12}$ line, shown in the middle panels of Fig. 19.

The H_3O^+ ion is another example of a species that is sensitive to pumping by far-infrared emission. Especially the $3_2^+ \rightarrow 2_2^-$ transition at 364 GHz is enhanced with respect to the other lines (Phillips, Van Dishoeck and Keene, 1992). This transition already depends on dust temperature at low values of $E(B - V)$, whereas pumping by dust radiation only starts to become important for the other transitions of H_3O^+ when higher amounts of dust are present.

10.3. *Effects of electron collisions*

Rates for collisions between molecules and electrons can be computed following the method described in Dickinson et al. (1977) for neutral species, and Dickinson & Flower (1981) for ions. They present an empirical fit to the collision strength, resulting in an equation for the collision rates.

Figure 20 shows plots for HCN and HCO^+ similar to Fig. 8, but this time including collisions with free electrons. The electron abundance is $X(\text{e}) = n(\text{e})/n(\text{H}_2) = 1 \times 10^{-4}$, which is higher than expected in any type of cloud studied in this work, but useful to illustrate the effects. For example, chemical calculations for a particular photon dominated region, IC 63 (Jansen et al. 1995; Chapter 4), give an electron fraction not higher than 1×10^{-5} , except at the edge of the cloud.

It is seen from the comparison between Figs. 8 and 20, that the effect on HCO^+ is rather small. Only in the $1 \rightarrow 0 / 4 \rightarrow 3$ ratio is the effect clearly visible. Therefore, the effect of collisions with electrons can safely be ignored for this molecule at all normal interstellar conditions.

The effect on the HCN molecule is more dramatic. A more careful analysis shows that this is almost completely due to an enhancement of the $1 \rightarrow 0$ line in the case of a high electron abundance. The ratios between higher lying lines are much less affected,

as can be seen in Fig. 21f. This is because the electron collision rates are almost equal for all transitions, whereas the H_2 (or He) collision rates increase with increasing J .

These same calculations have been carried out for other molecules as well. Most of them are even less affected than HCO^+ , since the electron collision rates scale with the dipole moment. In most interstellar clouds the ionization fraction is at least an order of magnitude lower than the value of 1×10^{-4} used here. Therefore, it is safe to assume that the molecular excitation in these clouds is not affected by the electrons. Even in the case of HCN there is hardly any detectable effect when the electron abundance is dropped to 1×10^{-5} . Only in diffuse and translucent clouds which have $X(\text{e}) \approx (1 - 5) \times 10^{-4}$ is the effect significant (Drdla et al. 1989).

The effects of electron collisions are most striking in these clouds at low total densities, in particular in enhancing the intensity of the lowest-lying transitions. The effect of electrons on the cm-wave transitions of formaldehyde has been well-known since some of the earliest discussions of its excitation (Thaddeus 1972).

10.4. Formaldehyde ortho / para exchange processes

The results shown so far have assumed for molecules with ortho and para varieties that the ratio between these varieties is at its equilibrium value in the high-temperature limit, i.e. determined by the statistical weights of the levels. Although the temperatures under consideration are not always high enough to justify the use of this limit, it can be argued on thermodynamical grounds that when a molecule like formaldehyde is formed by exoergic reactions, the formation distributes the molecules according to the statistical ortho / para ratio.

In order to further justify this assumption, calculations were performed for formaldehyde (H_2CO) which include ortho/para exchange reactions with a rate coefficient of 10^{-9} . Since these reactions require a collision with an H-bearing ion, the density of such collision partners is low, of the same order as the electron density. The value chosen for the calculations shown in Fig. 22 is $n(\text{ion}) = 1 \times 10^{-4} n(\text{H}_2)$, but as in the previous paragraph, the adopted value is higher than expected in normal interstellar clouds. For example, typical models of dense clouds give $n(\text{H}_3^+)/n(\text{H}_2) \lesssim 10^{-7}$. By comparing Fig. 22 to the corresponding panels of Figs. 9 and 10 it is clear that the differences for ratios within one ladder are small, of order 10%. However, when the ortho/para ratio changes due to exchange reactions, so will the cross-ladder line ratios.

10.5. Summary of temperature and density probes

It is often useful when planning observations to know which molecular lines are sensitive to a given temperature or density regime. On the one hand, the line ratio needs to show large variation over the expected range in the physical parameter that is to be measured, but on the other hand, both molecular lines should be observable with a sufficiently high signal-to-noise ratio.

The results of our findings are summarized in Figs. 5 and 6. Figure 5 shows which molecular lines are most useful to probe specific regimes in density. Figure 6 shows a similar picture for temperature probes. These figures assume that all lines are optically thin. Molecules such as CO, CS, HCO^+ , HCN and H_2CO are usually readily detectable in dense molecular clouds. Other species such as SiO, HC_3N and CH_3CN may depend more on the chemical conditions in the cloud.

It is seen from these figures that there are many lines that can be used as density and

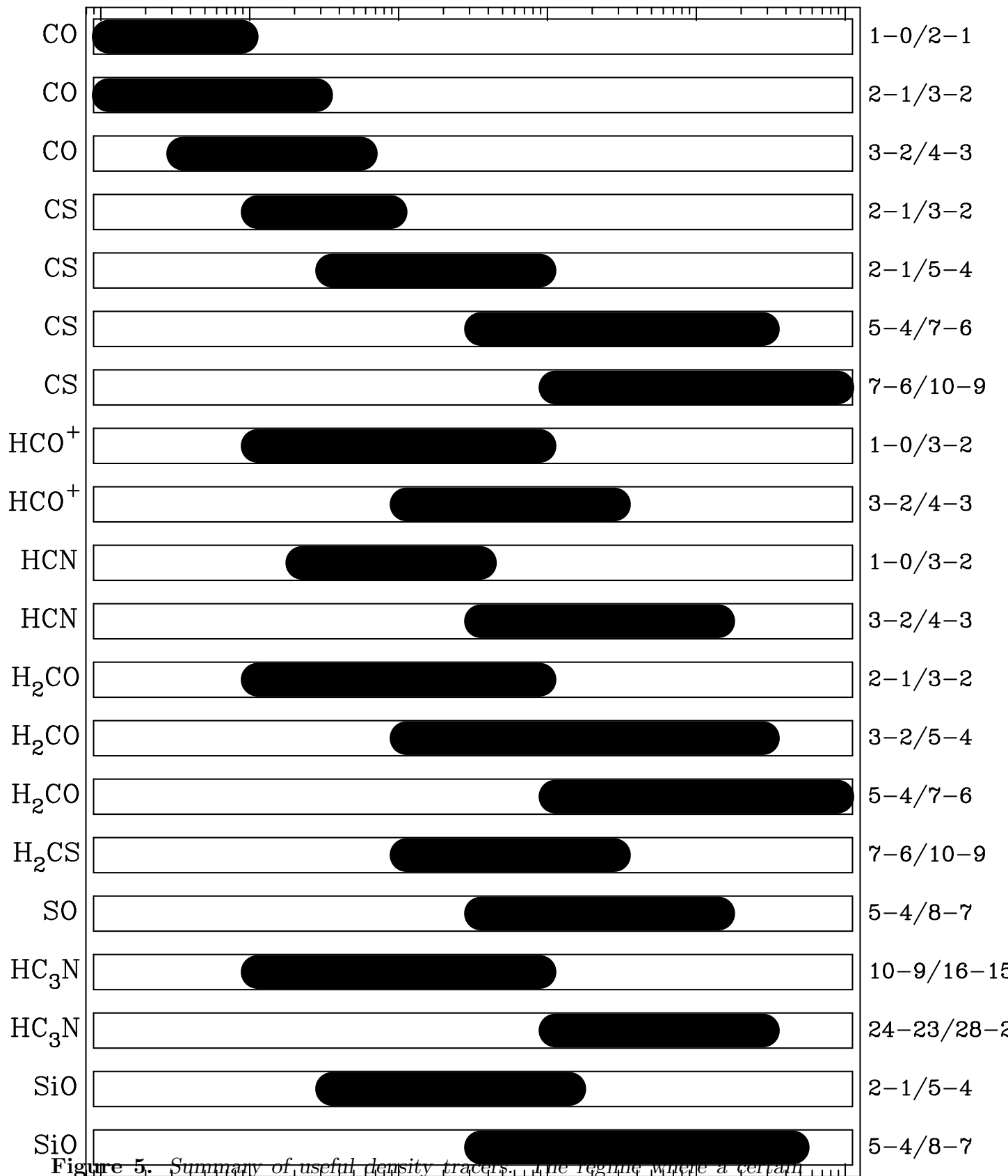


Figure 5. Summary of useful density tracers. The regime where a certain line ratio is sensitive is indicated with a solid bar. When this regime in density depends on temperature, it is shown for $T_{\text{kin}} = 80$ K.

$$n(\text{H}_2) \text{ (cm}^{-3}\text{)}$$

temperature probes if they can be observed. Only at the lowest densities ($n(\text{H}_2) \lesssim 1 \times 10^4 \text{ cm}^{-3}$) and temperatures ($T_{\text{kin}} \lesssim 35 \text{ K}$) is there a shortage of indicators, but for the range of temperatures present in the clouds studied in this work, molecules can be used as excellent tracers of the physical properties. Optically thick lines of CO are also useful temperature tracers if the source fills the beam of the

H_2CO

H_2CO

H_2CO

H_2CO

CH_3CN

CH_3CN

11. The young stellar object IRAS 16293 – 2422

As an example of the data analysis, the young stellar object IRAS 16293 – 2422 is chosen. It is a proto-binary star in the Ophiuchus cloud complex, with two dust continuum sources, both of mass $\approx 0.5 M_\odot$. The data used here were published in Blake et al. (1994) and Van Dishoeck et al. (1995).

The observations of species such as CS, SiO, H_2CO , and H_2CS indicate densities between $1 \times 10^6 \text{ cm}^{-3}$ and $1 \times 10^7 \text{ cm}^{-3}$ and are reasonably consistent among the various originate from the same part of the cloud. A more careful analysis (Van Dishoeck et al. 1995) shows, however, that different H_2CO lines trace different temperatures, and that other species, such as CN and C_2H , probe a lower density and temperature.

Also the H_2CO lines seem to trace a component with a much lower density $1 \times 10^4 \text{ cm}^{-3}$. This can be understood since these lines have a low critical density, and are thus not very sensitive to the higher densities. Thus, when a low density component is present, low- J CO lines will trace that component rather than tracing the bulk of the material. In the case of IRAS 16293 – 2422, this low density component is identified as the larger, circumbinary envelope in which the protostars are embedded. A similar

case is seen for the Orion Bar PDR (Hogerheijde et al. 1995; Chapter 6), where C¹⁸O emission from the dark cloud behind the PDR is observed.

Once the temperature and density have been constrained, one can try to match the observed intensities by varying the column density of the molecule. The validity of the assumption of optically thin lines can also be checked for the derived column density. In the case of IRAS 16293 – 2422 this is easily accomplished, since many isotopes have been observed. However, this falls outside the scope of the present chapter; the reader is referred to Blake et al. (1994) and Van Dishoeck et al. (1995) for the results on IRAS 16293 – 2422.

12. Conclusions

Rotational lines of simple molecules are excellent diagnostics for the physical parameters in interstellar space. Linear molecules often trace the density, whereas more complex molecules like H₂CO have transitions that are primarily sensitive to temperature. Ratios between lines of the same molecule provide an easy way to study the temperature and density, without being affected by molecular abundance variations. It has been shown that most species are not very sensitive to other parameters, such as dust emission and free electrons, so that these parameters may be ignored, leaving — in the optical thin case — only the dependence on temperature and density.

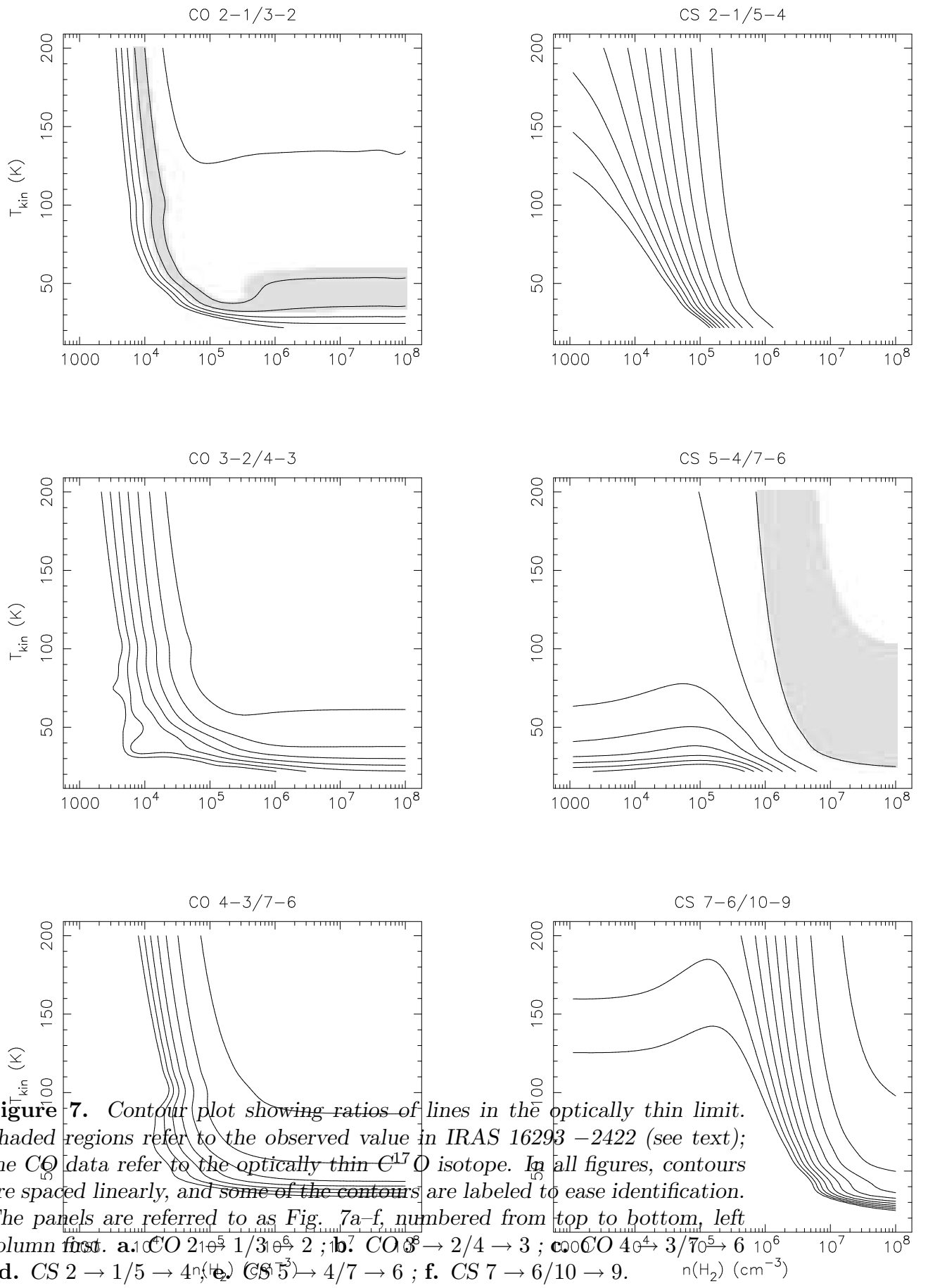
Homogeneous temperature and density models are of course a simplification of the actual situation. Usually one expects gradients or variations in the physical parameters to be present, which calls for more sophisticated models. Nevertheless, simple models such as those presented here often prove to be very useful as starting points.

The calculated line ratios have been compared with observations on the YSO IRAS 16293 – 2422. It is found that the molecular emission of species such as CS, SiO, H₂CO and H₂CS arises in a part of the source that is warm — $T_{\text{kin}} = 80$ K — and has a density in the range $1 \times 10^6 - 1 \times 10^7$ cm⁻³. From this it is seen that molecules can indeed be used to probe the temperature and density of warm, dense molecular clouds.

References

- Black, J.H., van Dishoeck, E.F., 1991, ApJ 369, L9
Blake, G.A., Van Dishoeck, E.F., Jansen, D.J., Groesbeck, T.D., Mundy, L.G., 1994, ApJ 428, 680
De Jong, T., Dalgarno, A., Boland, W., 1980, A&A 91, 68
Dickinson, A.S., Flower, D.R., 1981, MNRAS 196, 297
Dickinson, A.S., Phillips, T.G., Goldsmith, P.F., Percival, I.C., Richards, D., 1977, A&A 54, 645
Drdla, K., Knapp, G.R., van Dishoeck, E.F., 1989, ApJ 345, 815
Evans, N.J., 1980, in “Interstellar molecules”, IAU symposium 87 B.H. Andrew (ed.), Reidel, Dordrecht, p. 1
Flower, D.R., 1990, “Molecular collisions in the interstellar medium” Cambridge University Press, Cambridge
Flower, D.R., Launay, J.M., 1985, MNRAS 214, 271

- Genzel, R., 1992, in "The galactic interstellar medium", W.B. Burton, B.G. Elmegreen, R. Genzel (eds.), Springer, Berlin, p. 275
- Green, S., 1975a, ApJ 201, 366
- Green, S., 1975b, in "Atomic and molecular physics and the interstellar matter", North-Holland Publishing Co., Amsterdam, p. 83
- Green, S., Garrison, B.J., Lester, W.A., Miller, W.H., 1978, ApJS 37, 321
- Green, S., 1986, ApJ 309, 331
- Green, S., 1991, ApJS 76, 979
- Green, S., 1995, ApJS, in press
- Green, S., Chapman, S., 1978, ApJS 37, 168
- Green, S., Defrees, D.J., Mclean, A.D., 1987, ApJS 65, 175
- Green, S., Thaddeus, P., 1974, ApJ 191, 653
- Habing, H.J., 1988, in "Millimetre and submillimetre astronomy", Kluwer, Dordrecht, p. 207
- Hogerheijde, M., Jansen, D.J., Van Dishoeck, E.F., 1995, A&A 294, 792 (Chapter 6)
- Jansen, D.J., Van Dishoeck, E.F., Black, J.H., 1994, A&A 282, 605 (Chapter 3)
- Jansen, D.J., Van Dishoeck, E.F., Black, J.H., Spaans, M., Sosin, C., 1995, A&A, in press (Chapter 4)
- Monteiro, T.S., 1985, MNRAS 214, 419
- Monteiro, T.S., Stutzki, J., 1986, MNRAS 221, 33p
- Offer, A.R., Van Hemert, M.C., 1992, Chem. Phys. 163, 83
- Osterbrock, D.E., 1989, "Astrophysics of Gaseous Nebulae and Active Galactic Nuclei", University Science Books, Mill Valley
- Rybicki, G.B., Lightman, A.P., 1979, "Radiative processes in astrophysics", John Wiley & sons, New York
- Schinke, R., Engel, V., Buck, U., Meyer, H., Diercksen, G.H.F., 1985, ApJ 299, 939
- Sobolev, V.V., 1960, "Moving envelopes of stars", Harvard University Press, Cambridge
- Thaddeus, P., 1972, Ann. Rev. Astron. Astrophys. 10, 305
- Turner, B.E., Chan, K-W., Green, S., Lubowicz, D.A., 1992, ApJ 399, 114
- Van Dishoeck, E.F., Blake, G.A., Jansen, D.J., Groesbeck, T.D., 1995, ApJ, in press
- Walmsley, C.M., 1987, in "Physical processes in interstellar clouds", G.E. Morfill & M. Scholer (eds.), Reidel, Dordrecht, p. 161



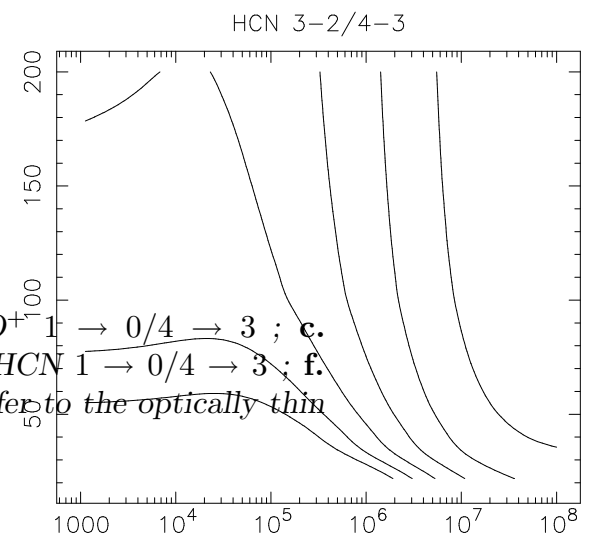
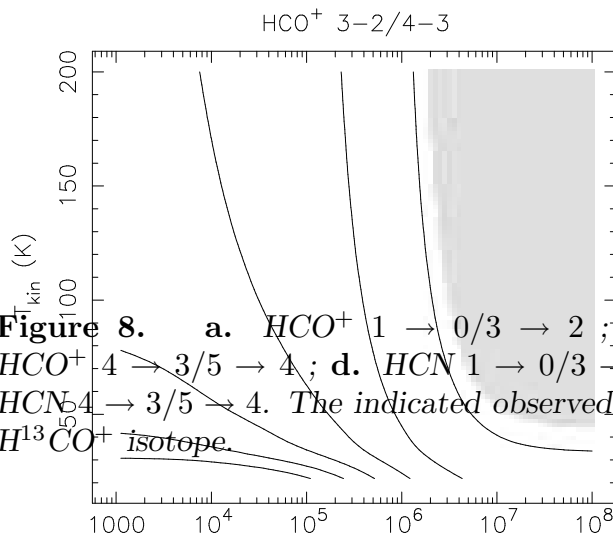
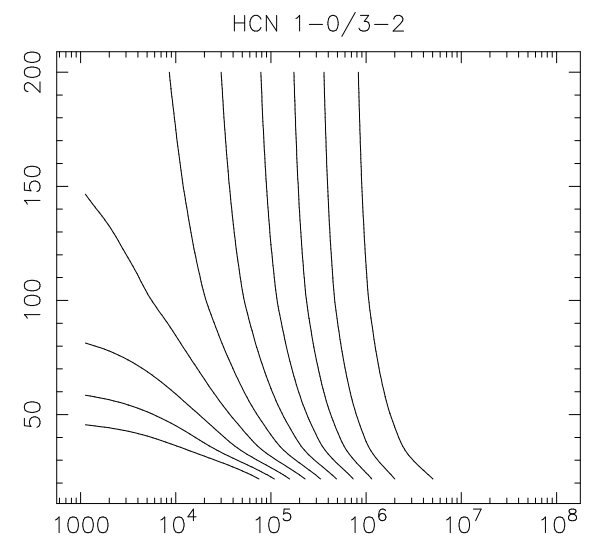
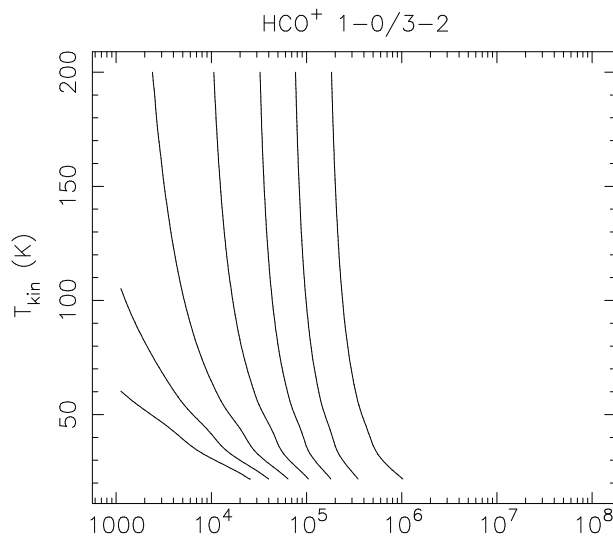
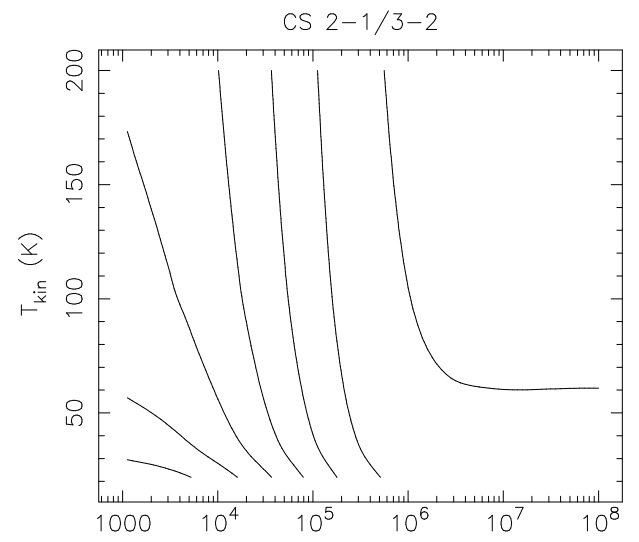
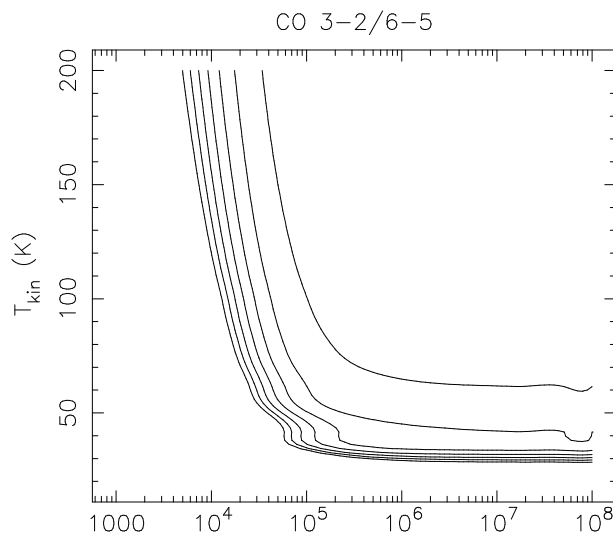


Figure 8. a. HCO^+ $1 \rightarrow 0/3 \rightarrow 2$; b. HCO^+ $1 \rightarrow 0/4 \rightarrow 3$; c. HCO^+ $4 \rightarrow 3/5 \rightarrow 4$; d. HCN $1 \rightarrow 0/3 \rightarrow 2$; e. HCN $1 \rightarrow 0/4 \rightarrow 3$; f. HCN $4 \rightarrow 3/5 \rightarrow 4$. The indicated observed values refer to the optically thin H^{13}CO^+ isotope.

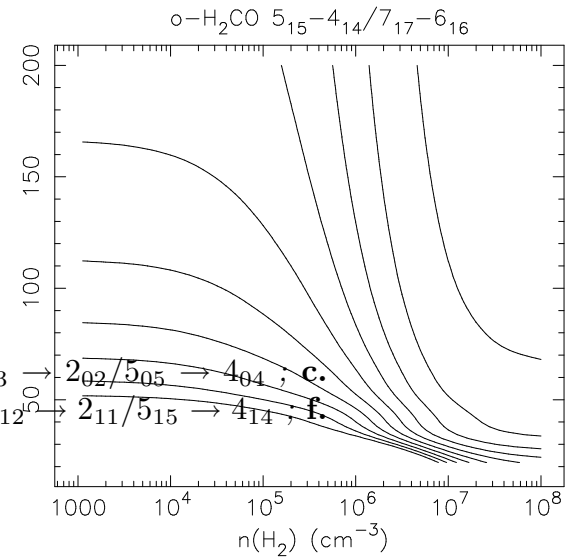
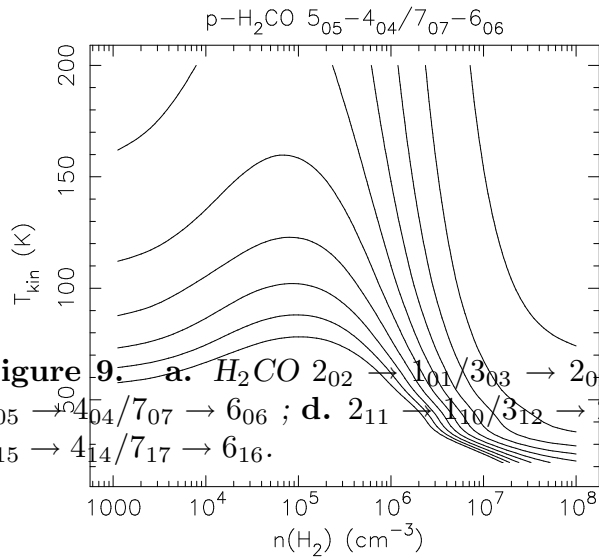
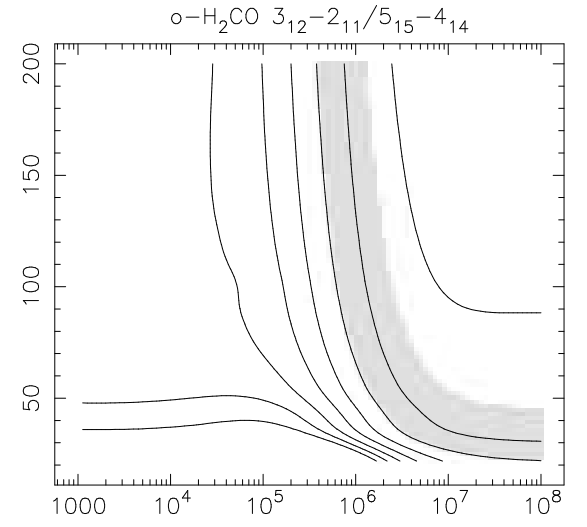
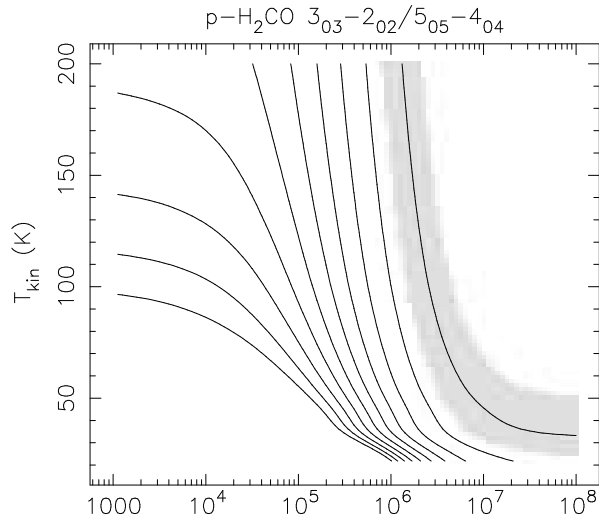
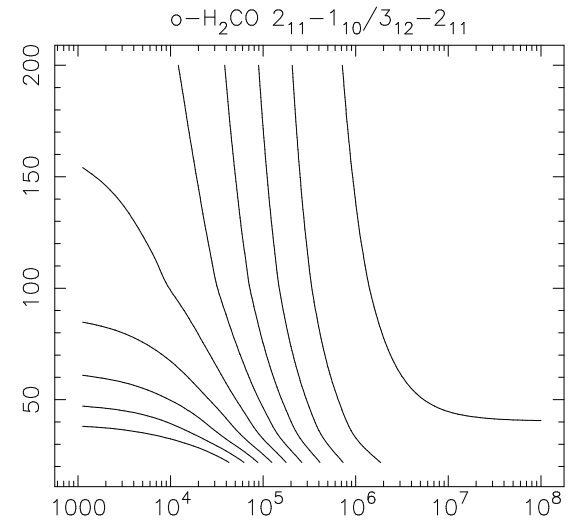
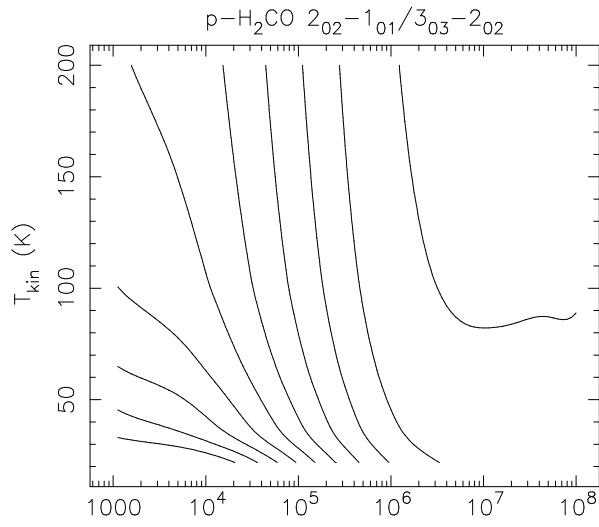


Figure 9. **a.** H_2CO $2_{02} \rightarrow 1_{01}/3_{03} \rightarrow 2_{02}$; **b.** $3_{03} \rightarrow 2_{02}/5_{05} \rightarrow 4_{04}$; **c.** $5_{05} \rightarrow 4_{04}/7_{07} \rightarrow 6_{06}$; **d.** $2_{11} \rightarrow 1_{10}/3_{12} \rightarrow 2_{11}$; **e.** $3_{12} \rightarrow 2_{11}/5_{15} \rightarrow 4_{14}$; **f.** $5_{15} \rightarrow 4_{14}/7_{17} \rightarrow 6_{16}$.

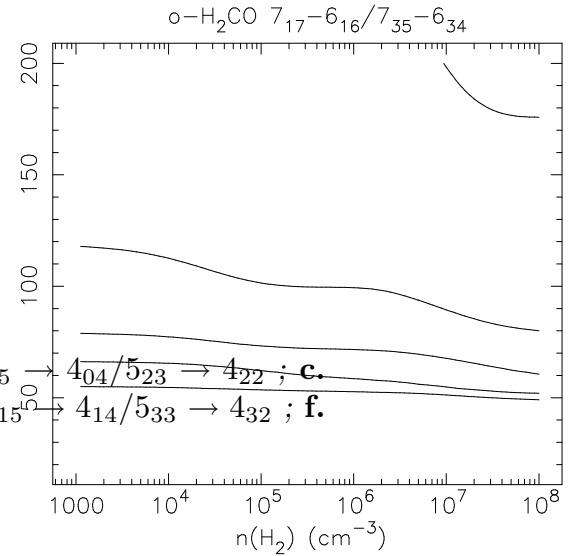
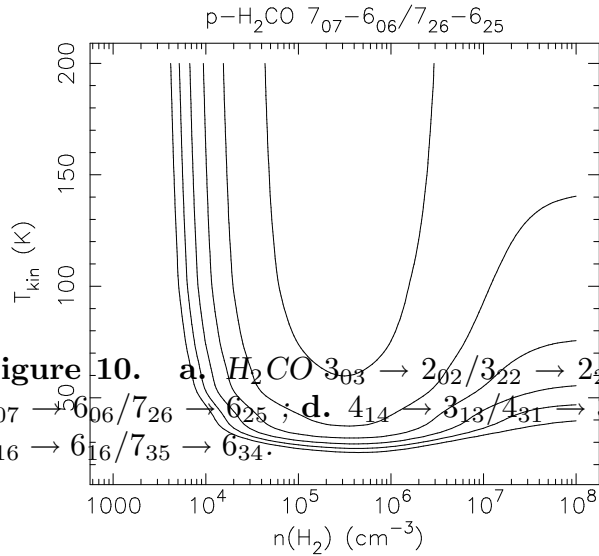
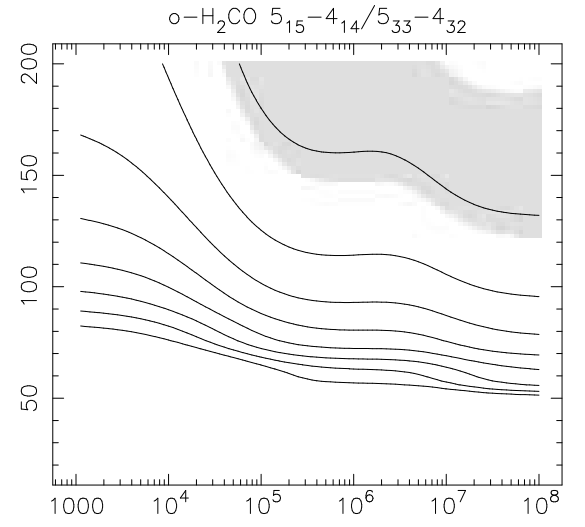
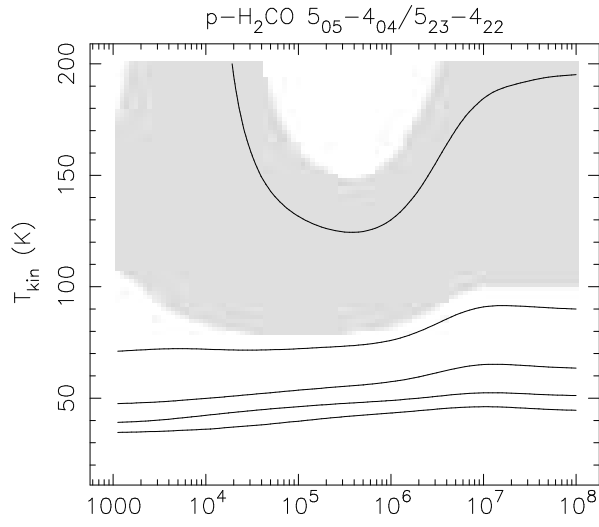
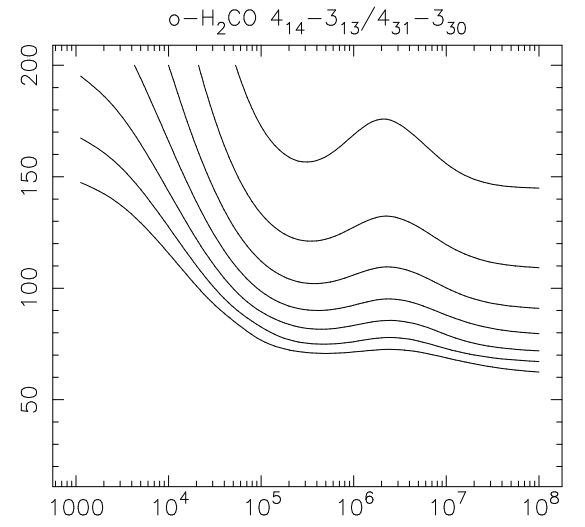
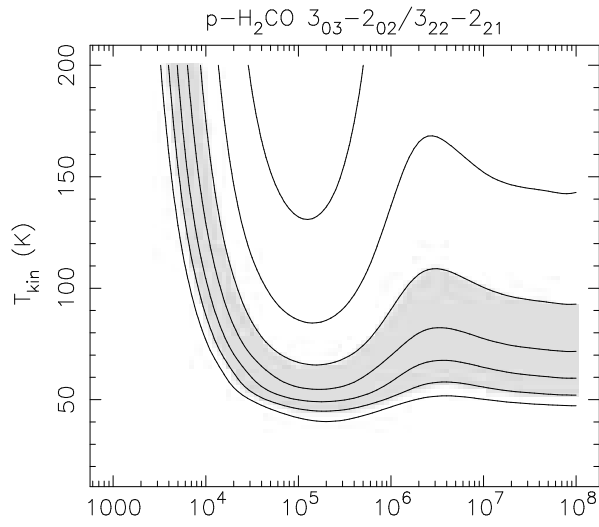


Figure 10. **a.** H_2CO $3_{03} \rightarrow 2_{02}/3_{22} \rightarrow 2_{21}$; **b.** $5_{05} \rightarrow 4_{04}/5_{23} \rightarrow 4_{22}$; **c.** $7_{07} \rightarrow 6_{06}/7_{26} \rightarrow 6_{25}$; **d.** $4_{14} \rightarrow 3_{13}/4_{31} \rightarrow 3_{30}$; **e.** $5_{15} \rightarrow 4_{14}/5_{33} \rightarrow 4_{32}$; **f.** $7_{17} \rightarrow 6_{16}/7_{35} \rightarrow 6_{34}$.

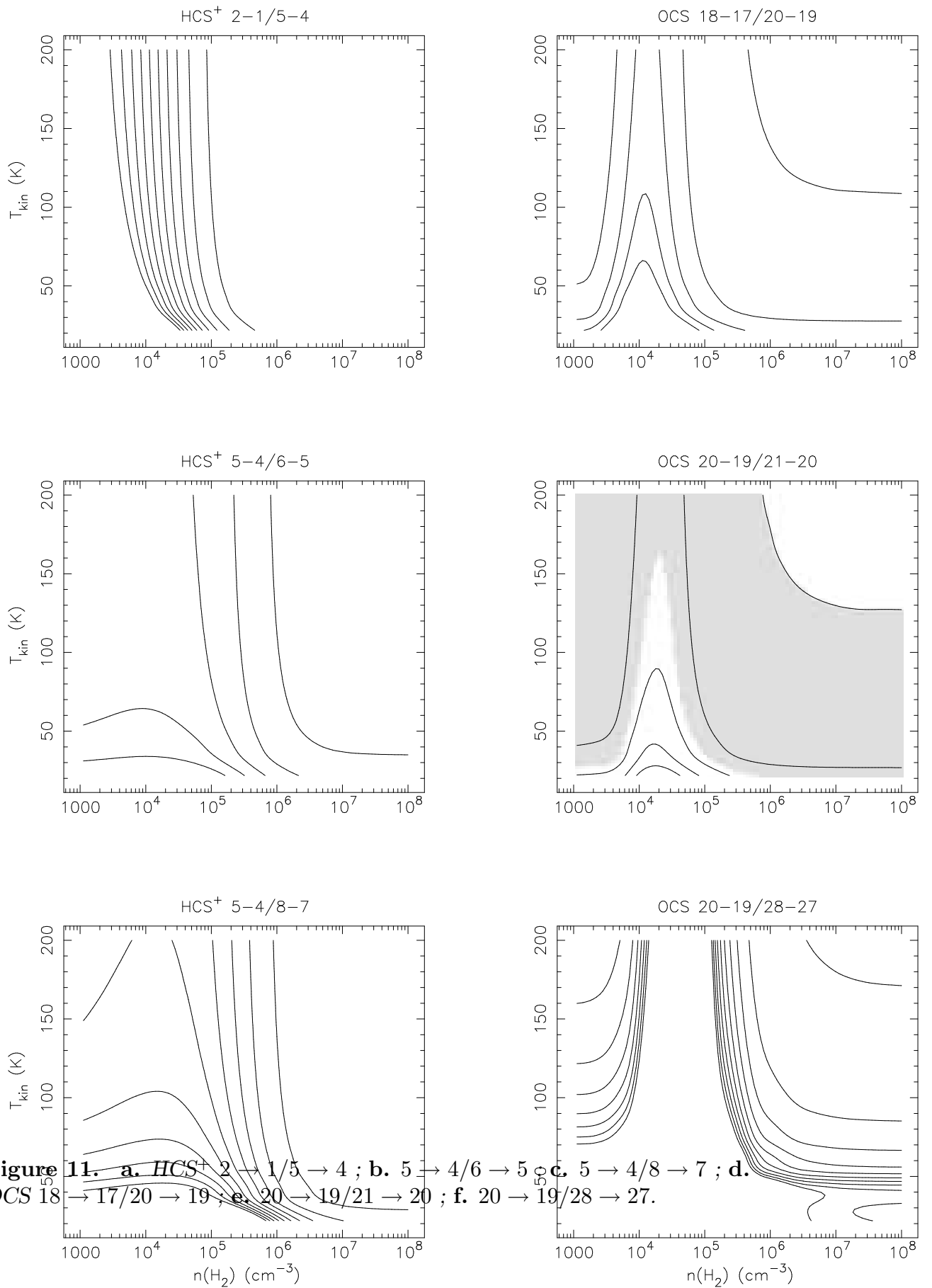


Figure 11. a. HCS^+ 2 \rightarrow 1/5 \rightarrow 4 ; b. 5 \rightarrow 4/6 \rightarrow 5 ; c. 5 \rightarrow 4/8 \rightarrow 7 ; d. OCS 18 \rightarrow 17/20 \rightarrow 19 ; e. 20 \rightarrow 19/21 \rightarrow 20 ; f. 20 \rightarrow 19/28 \rightarrow 27.

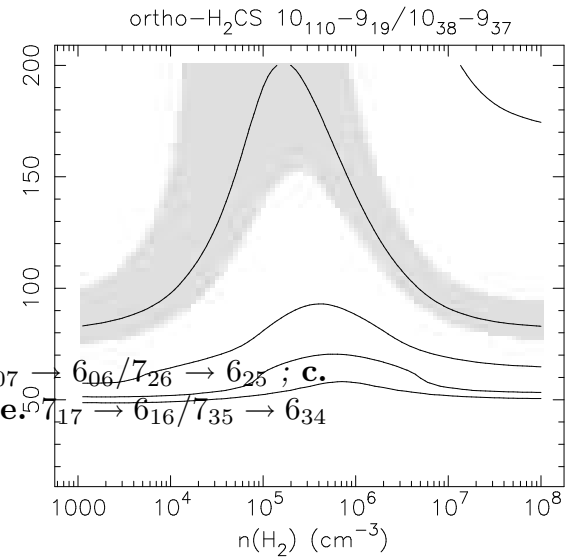
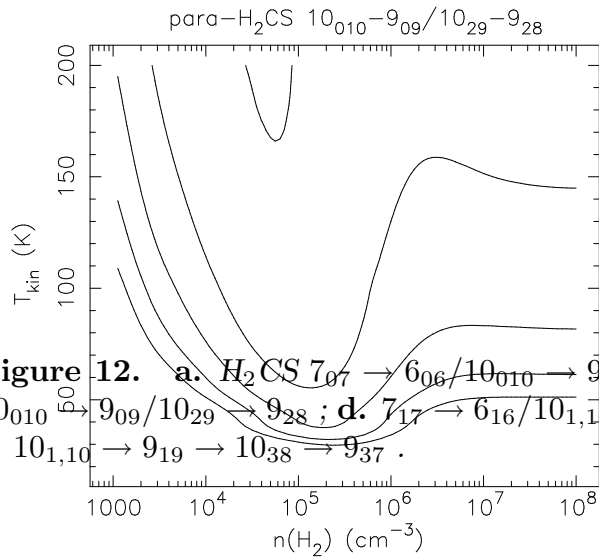
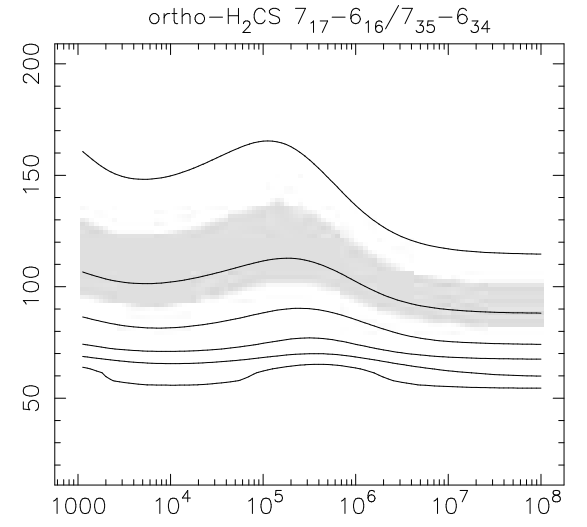
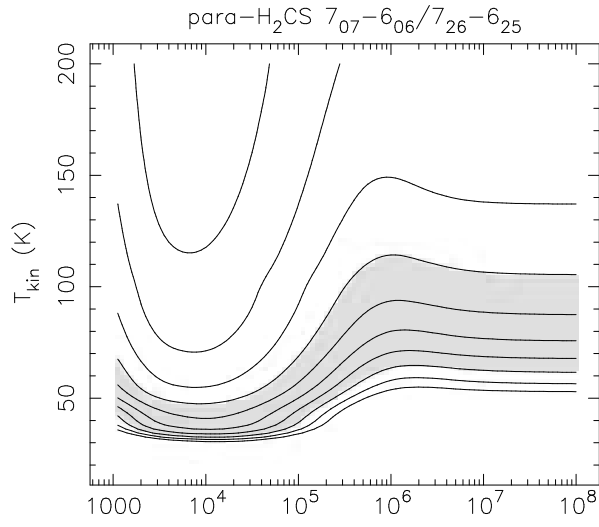
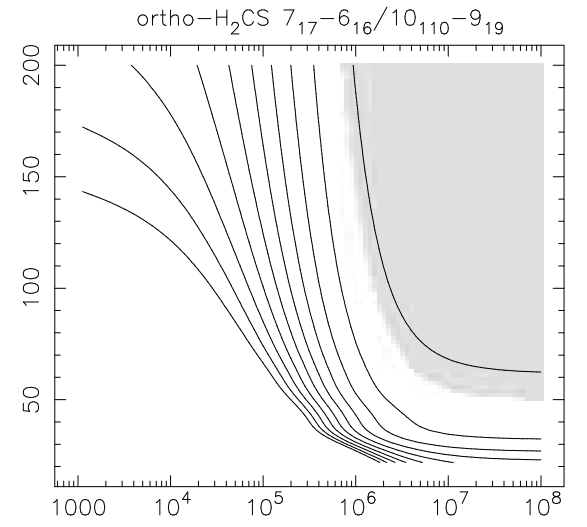
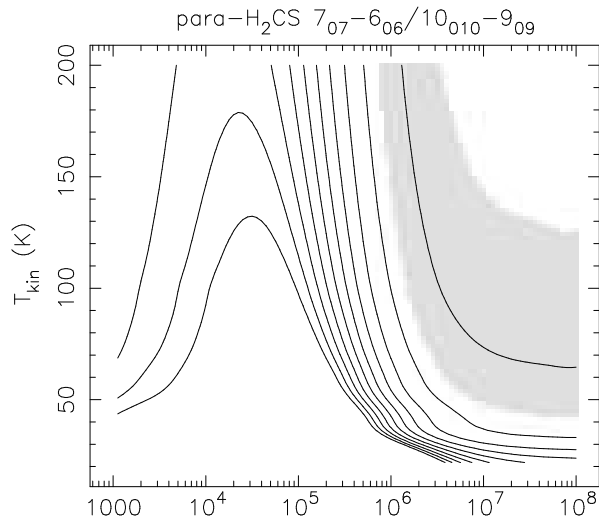


Figure 12. **a.** $\text{H}_2\text{CS } 7_{07} \rightarrow 6_{06}/10_{010} \rightarrow 9_{09}$; **b.** $7_{07} \rightarrow 6_{06}/7_{26} \rightarrow 6_{25}$; **c.** $10_{010} \rightarrow 9_{09}/10_{29} \rightarrow 9_{28}$; **d.** $7_{17} \rightarrow 6_{16}/10_{110} \rightarrow 9_{19}$; **e.** $7_{17} \rightarrow 6_{16}/7_{35} \rightarrow 6_{34}$; **f.** $10_{110} \rightarrow 9_{19}/10_{38} \rightarrow 9_{37}$.

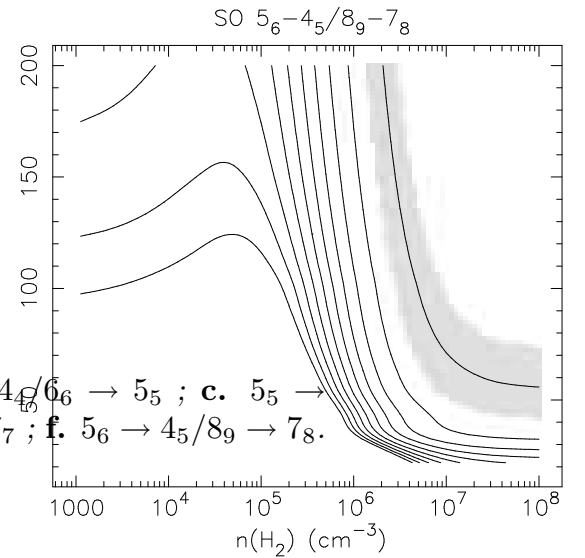
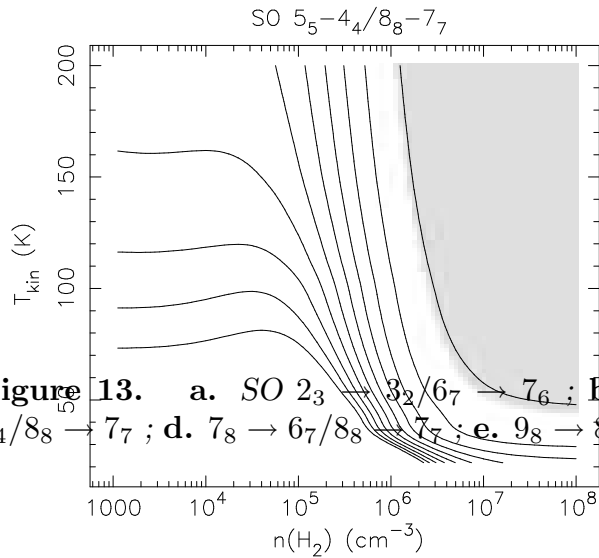
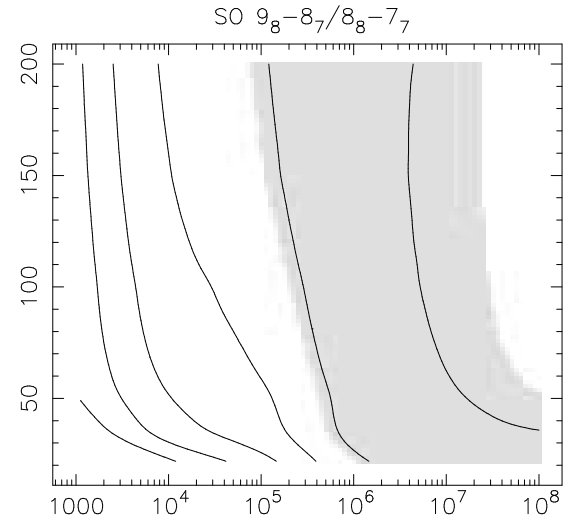
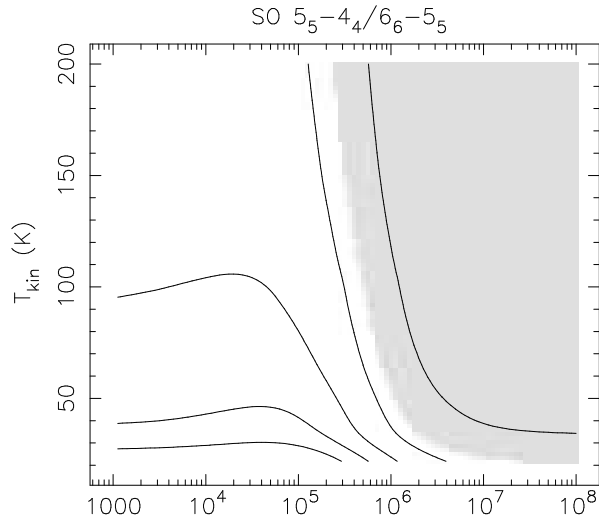
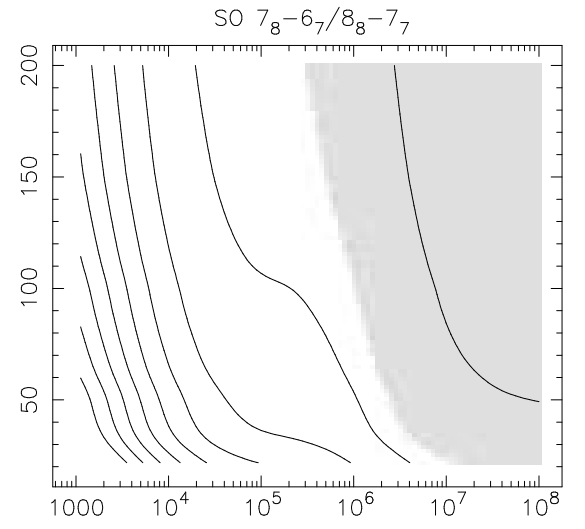
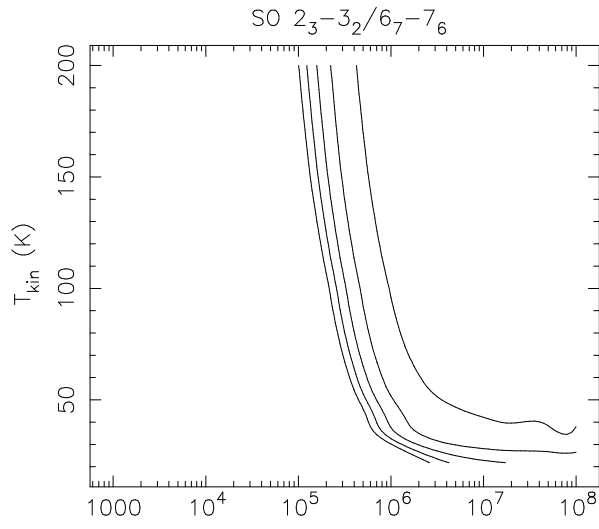


Figure 13. **a.** $SO\ 2_3 \rightarrow 3_2/6_7 \rightarrow 7_6$; **b.** $5_5 \rightarrow 4_4/6_6 \rightarrow 5_5$; **c.** $5_5 \rightarrow 4_4/8_8 \rightarrow 7_7$; **d.** $7_8 \rightarrow 6_7/8_8 \rightarrow 7_7$; **e.** $9_8 \rightarrow 8_7/8_8 \rightarrow 7_7$; **f.** $5_6 \rightarrow 4_5/8_9 \rightarrow 7_8$.

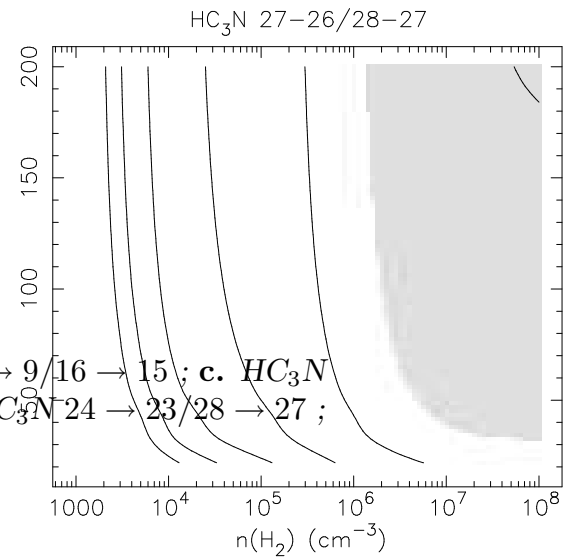
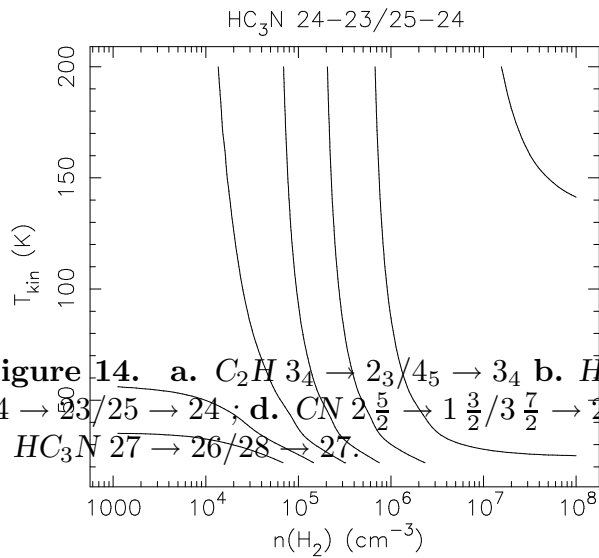
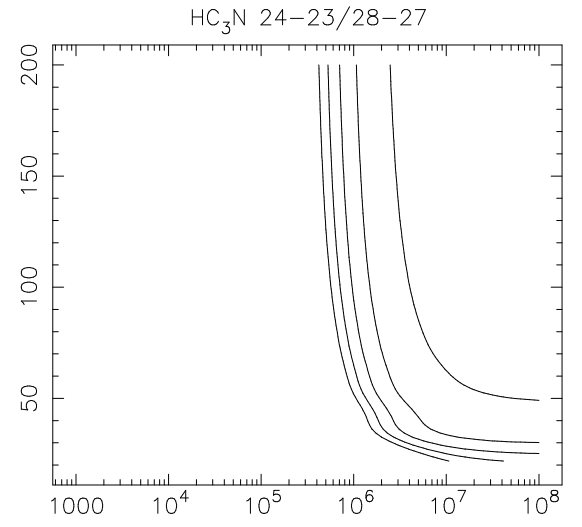
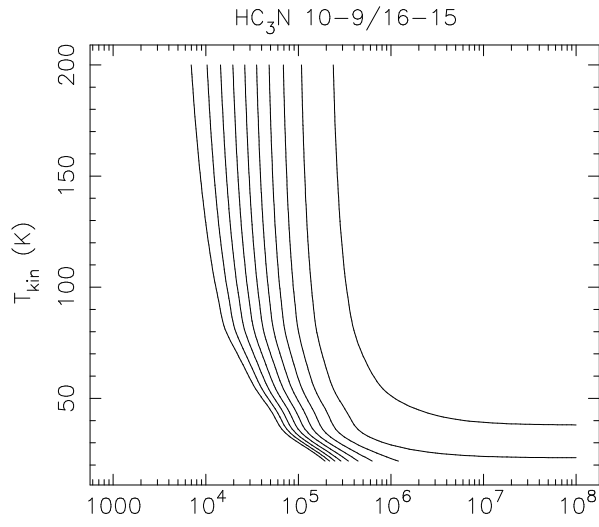
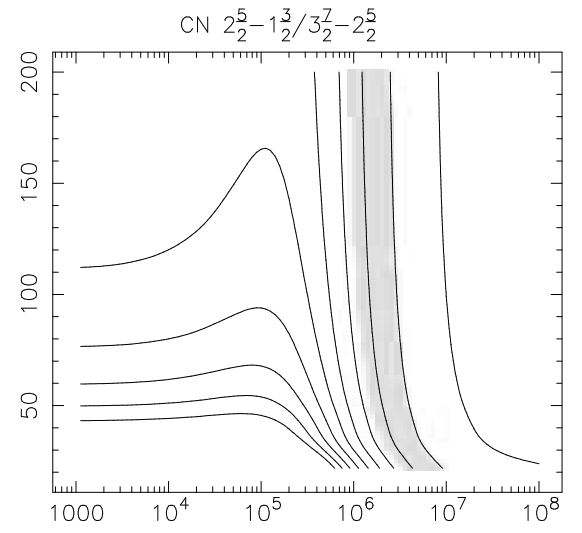
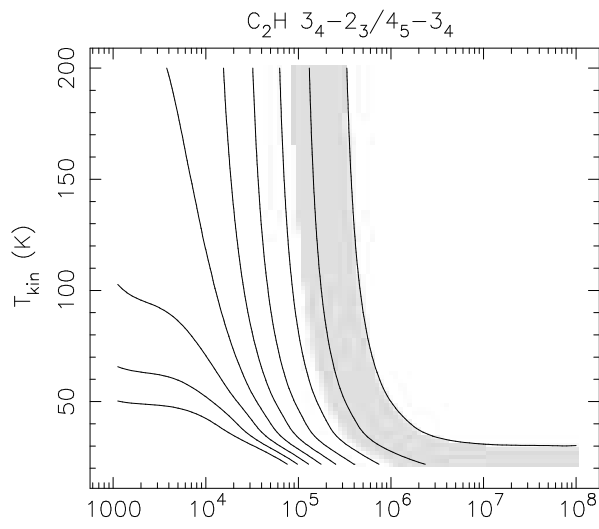


Figure 14. a. C_2H $3_4 \rightarrow 2_3/4_5 \rightarrow 3_4$ b. HC_3N $10 \rightarrow 9/16 \rightarrow 15$; c. HC_3N $24 \rightarrow 23/25 \rightarrow 24$; d. CN $2_{2}^{5} \rightarrow 1_{2}^{3}/3_{2}^{7} \rightarrow 2_{2}^{5}$; e. HC_3N $24 \rightarrow 23/28 \rightarrow 27$; f. HC_3N $27 \rightarrow 26/28 \rightarrow 27$.

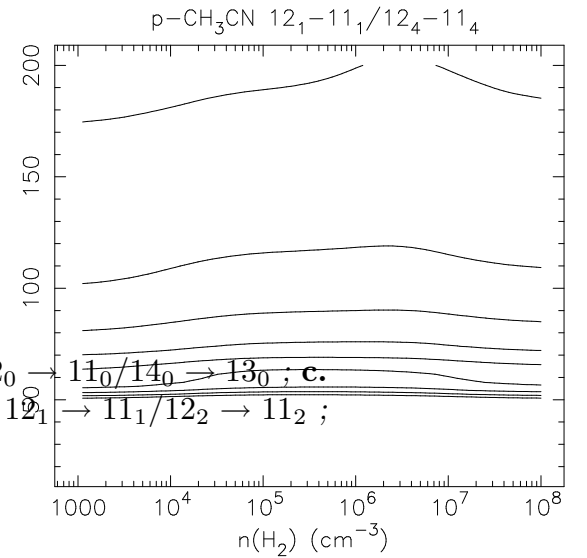
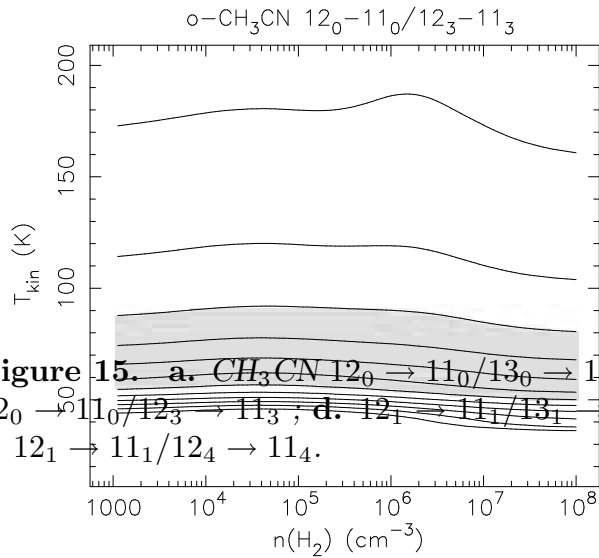
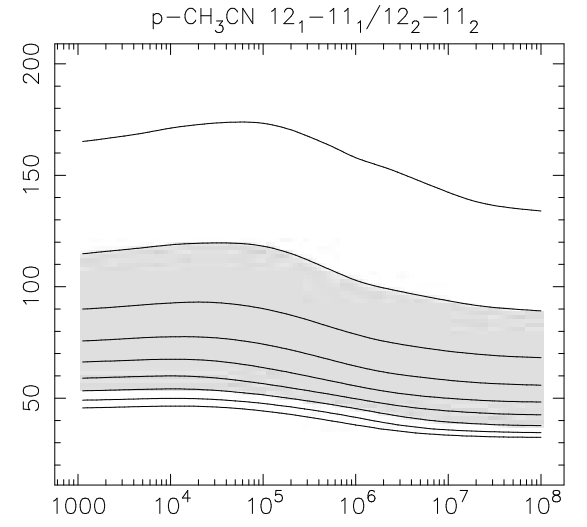
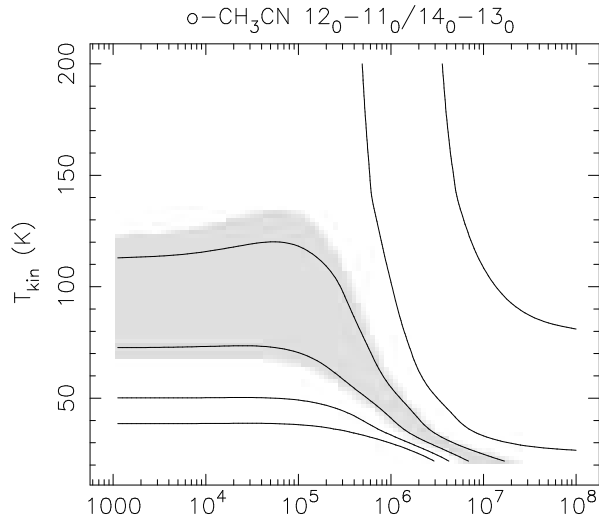
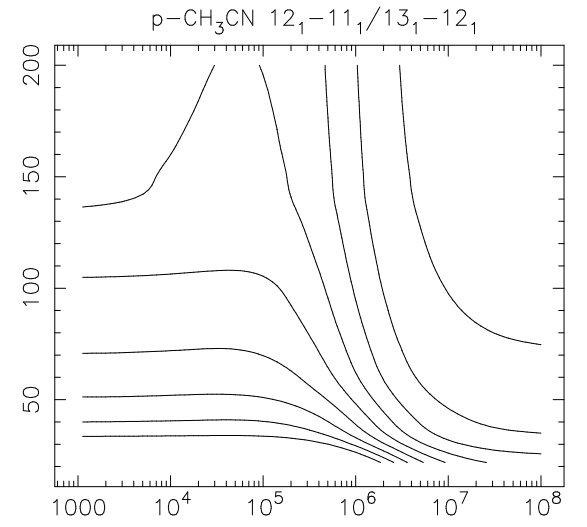
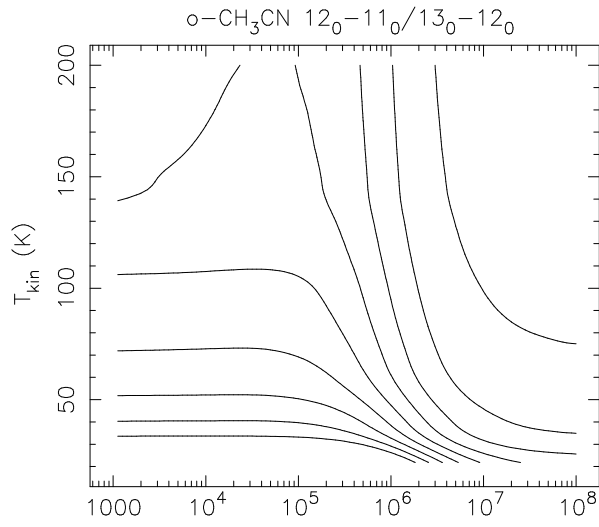
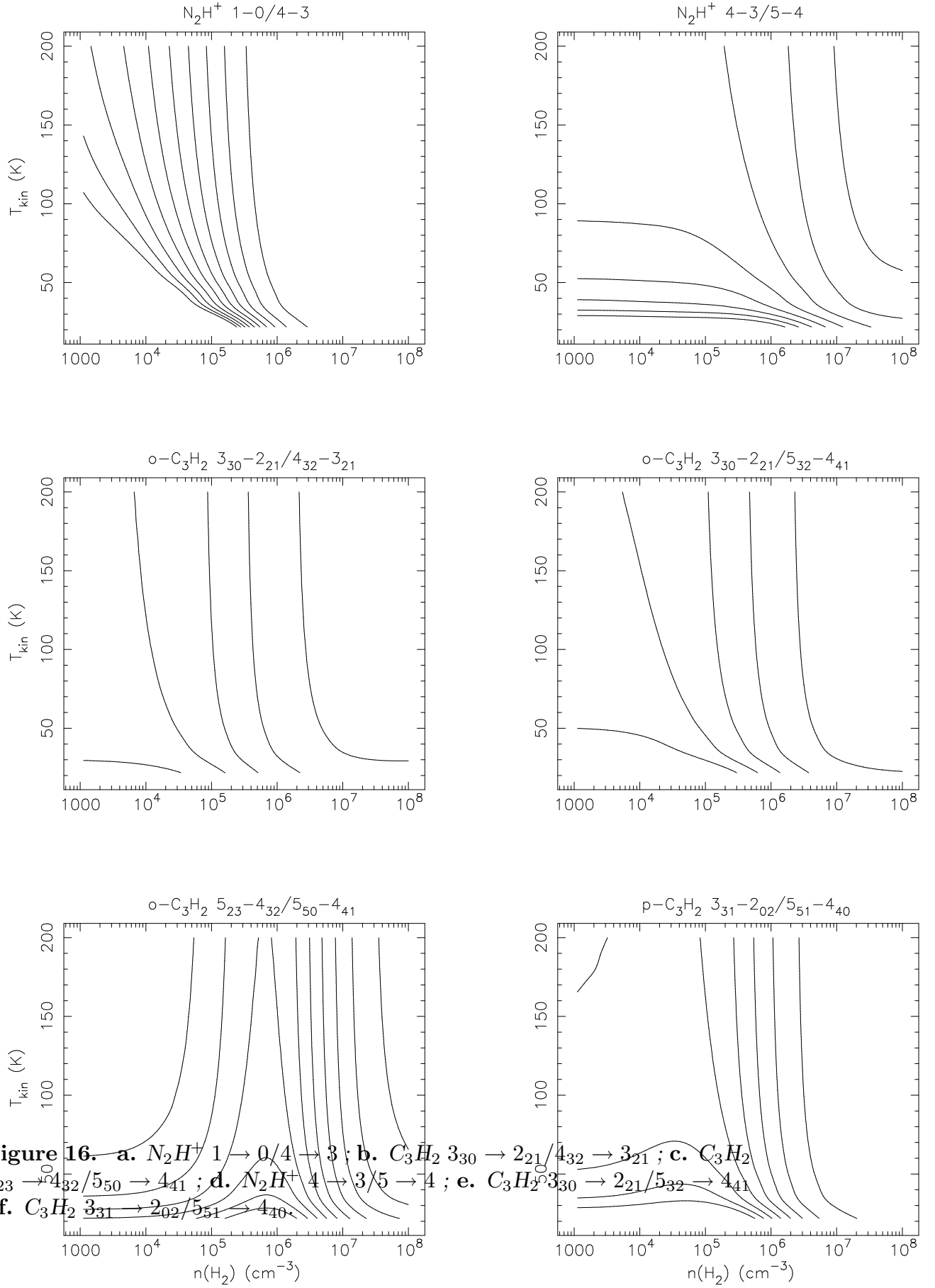


Figure 15. a. $\text{CH}_3\text{CN } 12_0 \rightarrow 11_0/13_0 \rightarrow 12_0$; b. $12_0 \rightarrow 11_0/14_0 \rightarrow 13_0$; c. $12_0 \rightarrow 11_0/12_3 \rightarrow 11_3$; d. $12_1 \rightarrow 11_1/13_1 \rightarrow 12_1$; e. $12_1 \rightarrow 11_1/12_2 \rightarrow 11_2$; f. $12_1 \rightarrow 11_1/12_4 \rightarrow 11_4$.



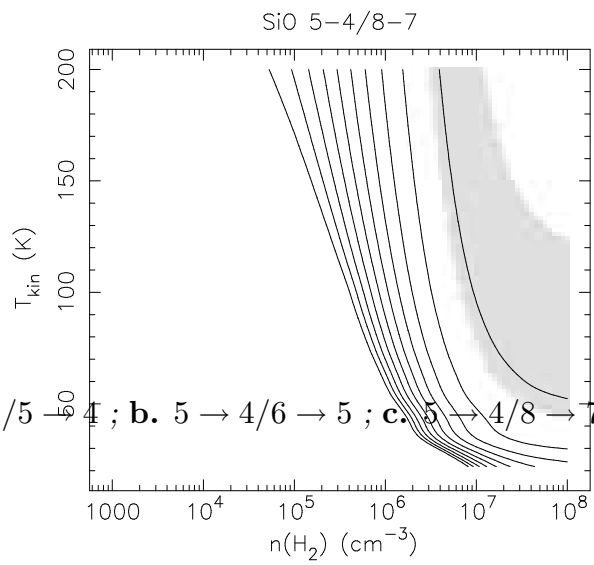
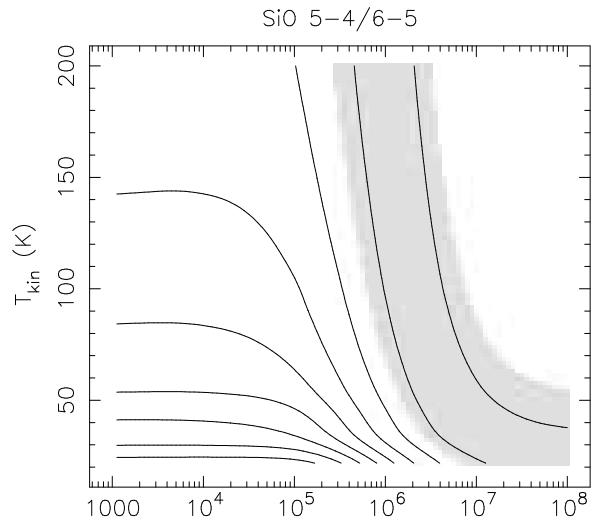
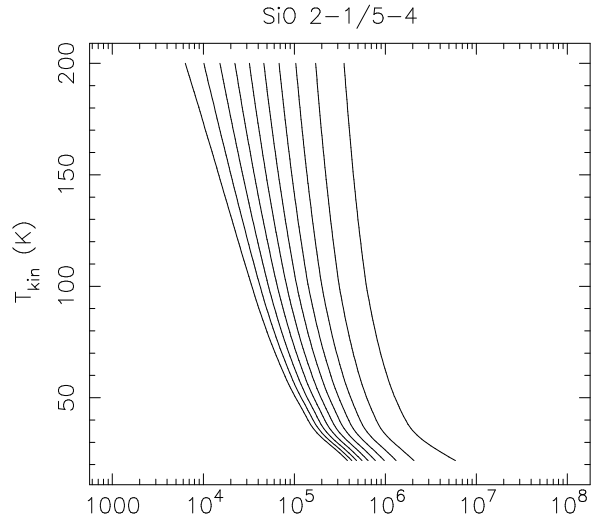


Figure 17. a. SiO $2 \rightarrow 1/5 \rightarrow 4$; b. $5 \rightarrow 4/6 \rightarrow 5$; c. $5 \rightarrow 4/8 \rightarrow 7$.

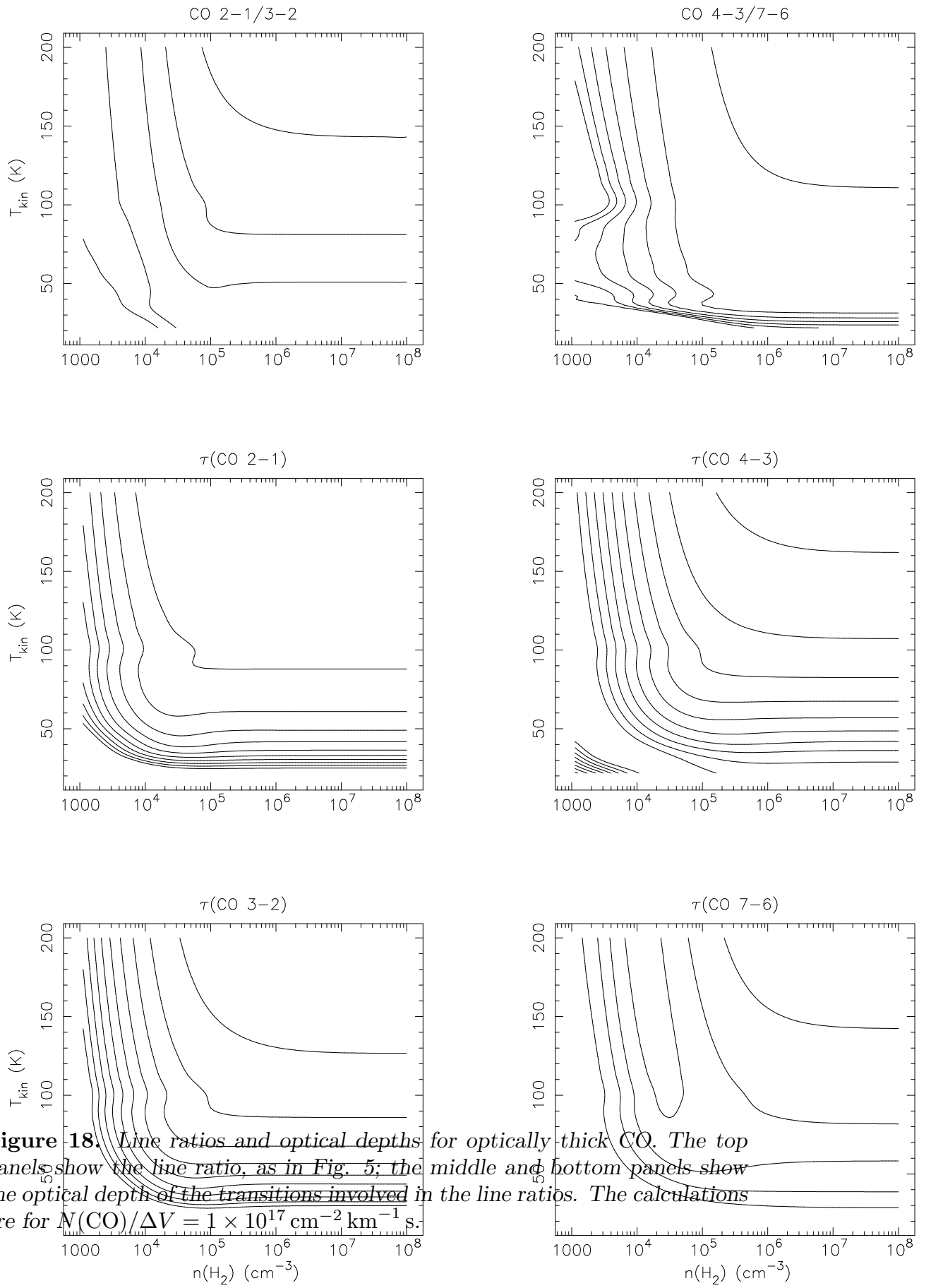


Figure 18. Line ratios and optical depths for optically thick CO. The top panels show the line ratio, as in Fig. 5; the middle and bottom panels show the optical depth of the transitions involved in the line ratios. The calculations are for $N(\text{CO})/\Delta V = 1 \times 10^{17} \text{ cm}^{-2} \text{ km}^{-1} \text{ s}$.

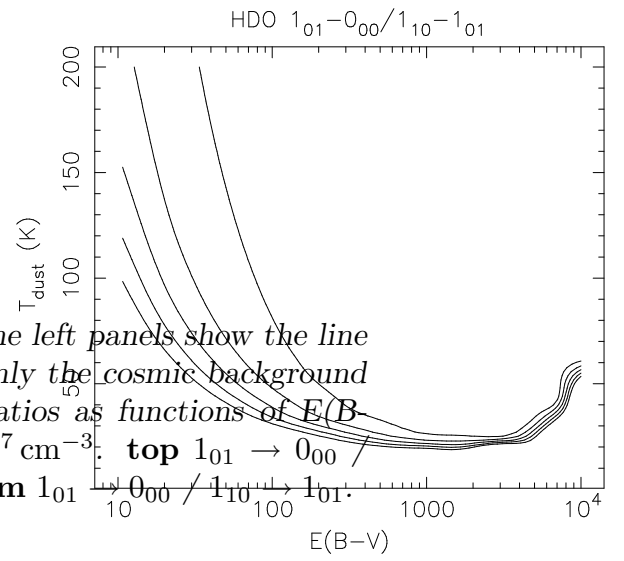
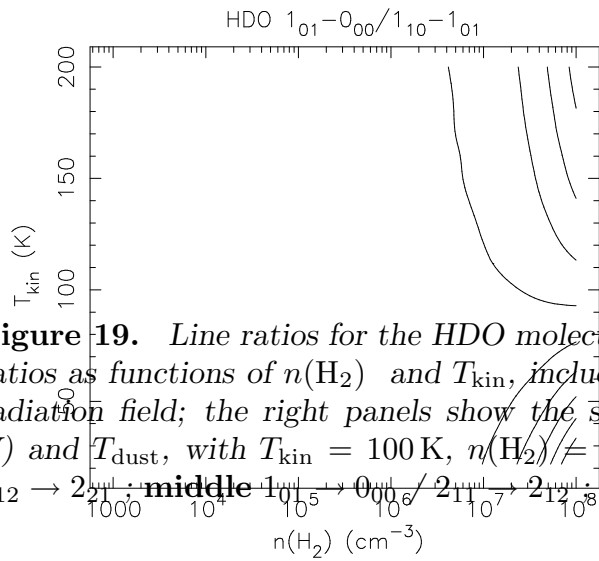
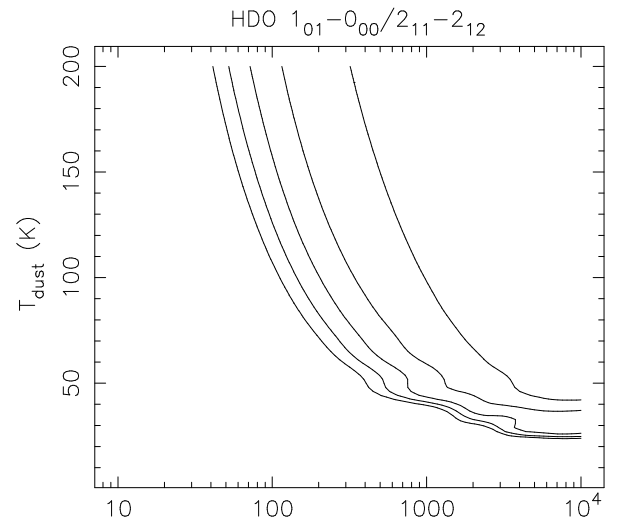
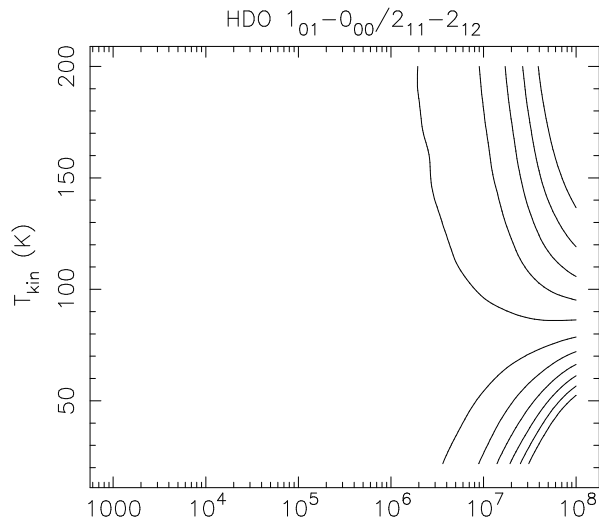
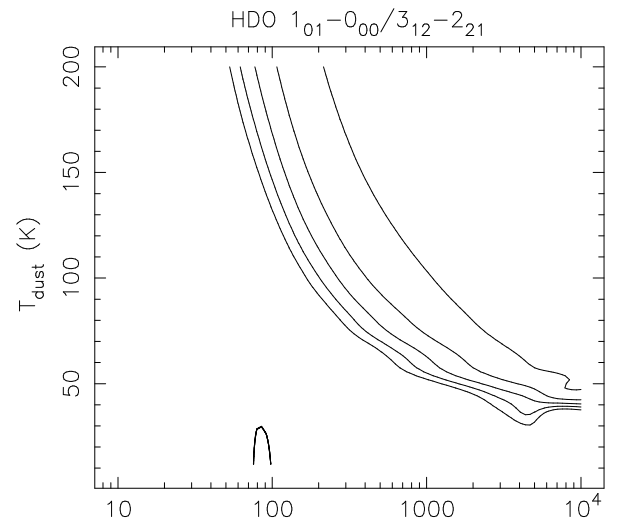
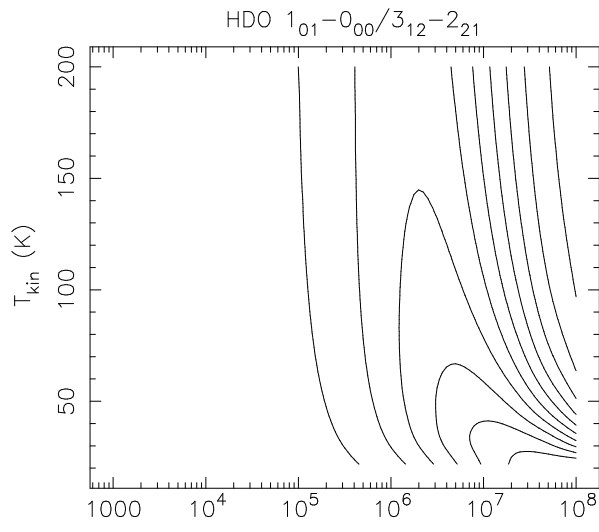


Figure 19. Line ratios for the HDO molecule. The left panels show the line ratios as functions of $n(\text{H}_2)$ and T_{kin} , including only the cosmic background radiation field; the right panels show the same ratios as functions of $E(B-V)$ and T_{dust} , with $T_{\text{kin}} = 100 \text{ K}$, $n(\text{H}_2) = 1 \times 10^7 \text{ cm}^{-3}$. **top** $1_{01} \rightarrow 0_{00} / 3_{12} \rightarrow 2_{21}$; **middle** $1_{01} \rightarrow 0_{00} / 2_{11} \rightarrow 2_{12}$; **bottom** $1_{01} \rightarrow 0_{00} / 1_{10} \rightarrow 1_{01}$.

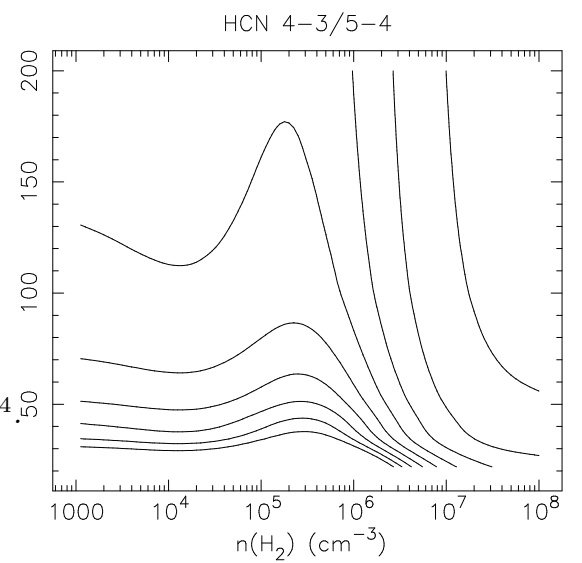
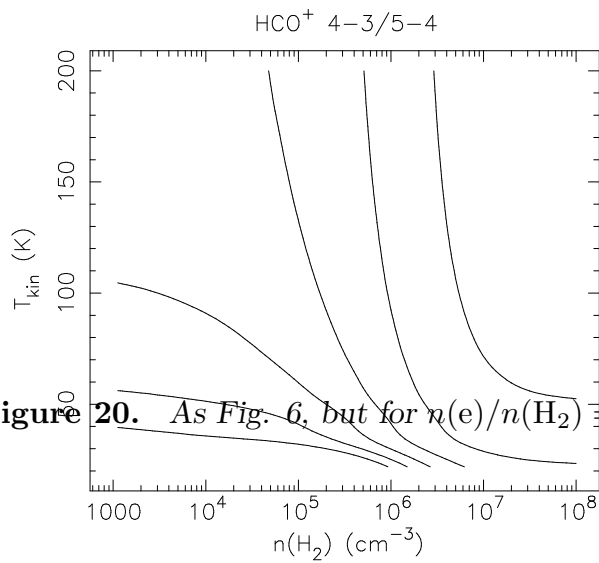
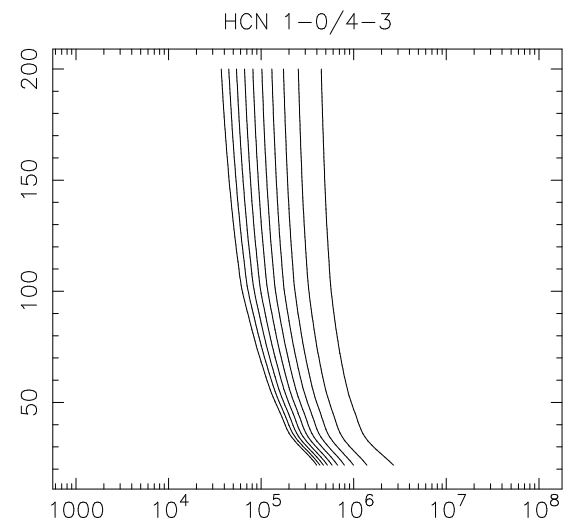
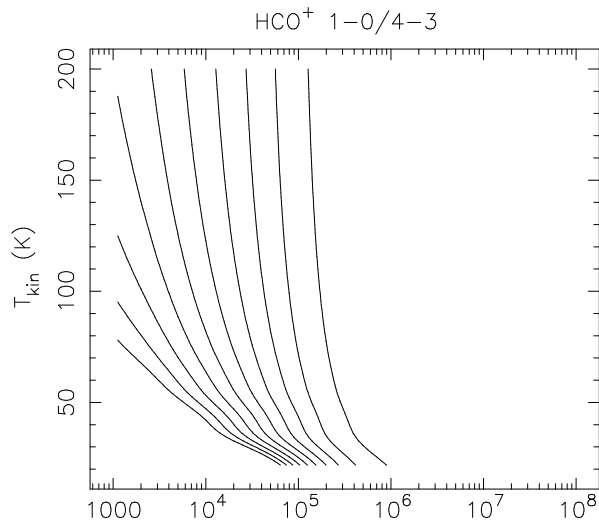
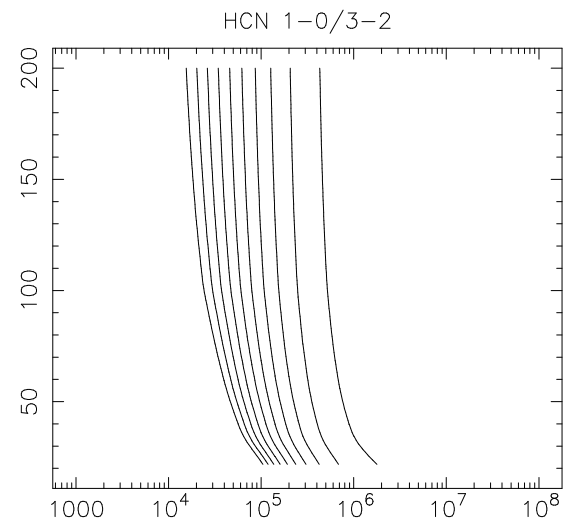
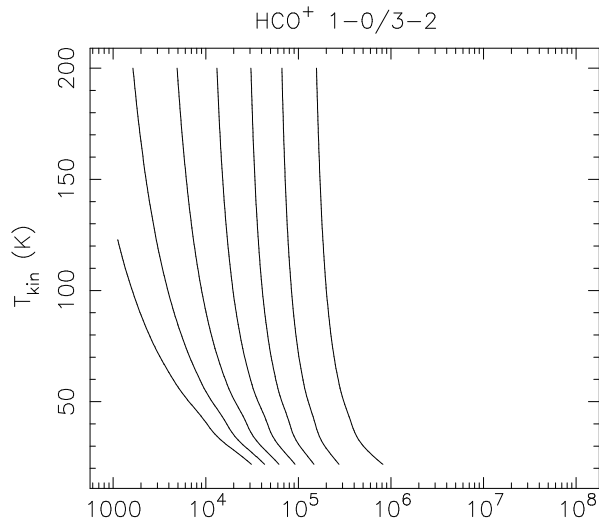


Figure 20. As Fig. 6, but for $n(e)/n(H_2) = 1 \times 10^{-4}$.

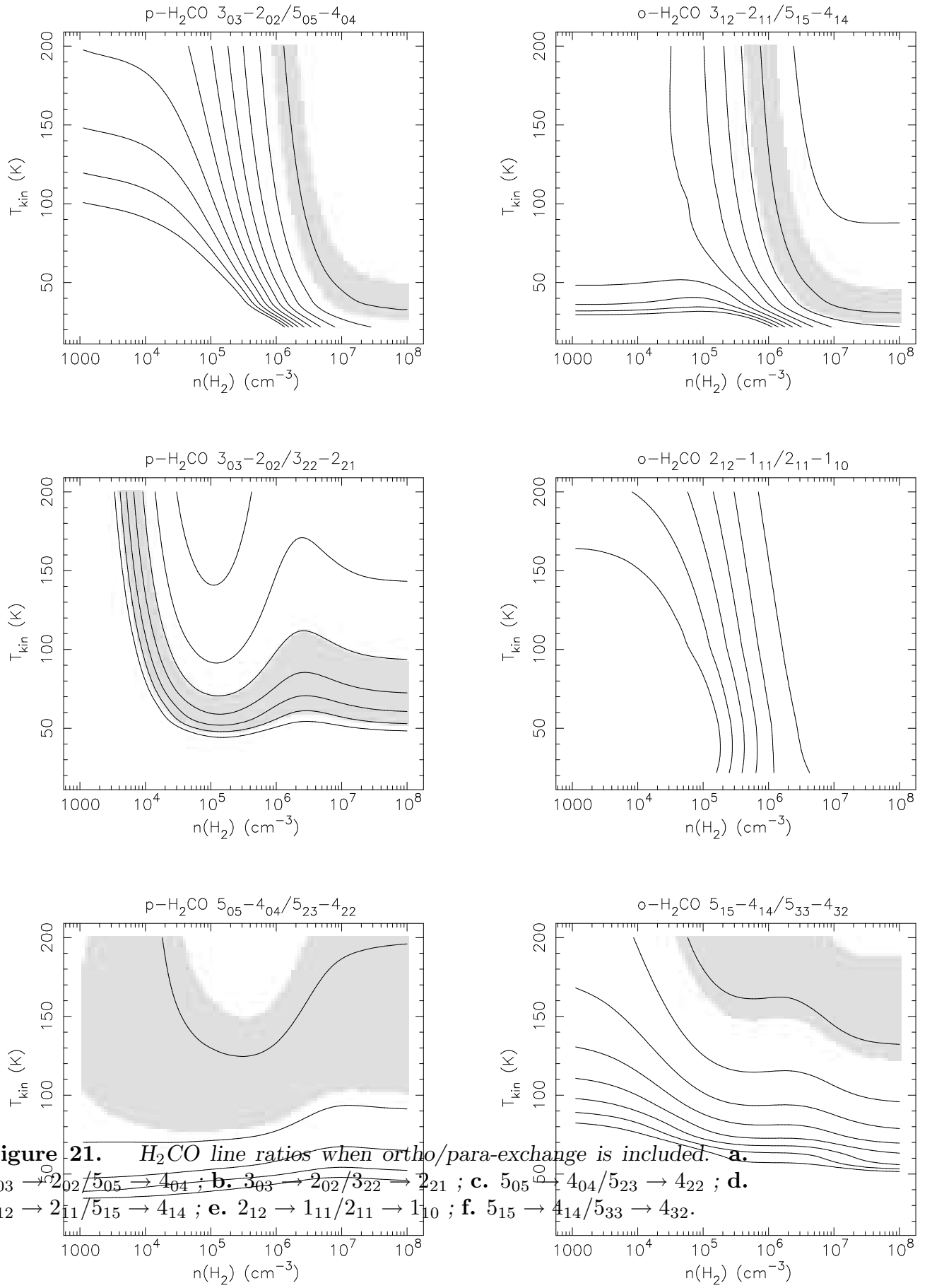


Figure 21. H_2CO line ratios when ortho/para-exchange is included. **a.** $3_{03} \rightarrow 2_{02}/5_{05} \rightarrow 4_{04}$; **b.** $3_{03} \rightarrow 2_{02}/3_{22} \rightarrow 2_{21}$; **c.** $5_{05} \rightarrow 4_{04}/5_{23} \rightarrow 4_{22}$; **d.** $3_{12} \rightarrow 2_{11}/5_{15} \rightarrow 4_{14}$; **e.** $2_{12} \rightarrow 1_{11}/2_{11} \rightarrow 1_{10}$; **f.** $5_{15} \rightarrow 4_{14}/5_{33} \rightarrow 4_{32}$.